Title: T cell Aryl Hydrocarbon Receptor Activity Tunes the Gut Microenvironment to Sustain Autoimmunity and Neuroinflammation.

Short Title: T cell AHR and neuroinflammation

Authors: Andrea R. Merchak,[1, 2, 3] Hannah J. Cahill,[1] Lucille C. Brown,[1] Ryan M. Brown,[1,2, 3] Courtney Rivet-Noor,[1,2, 3] Rebecca M. Beiter,[1,2, 3] Erica R. Slogar,[1] Deniz G. Olgun,[1] and Alban Gaultier[1, 3]*

Affiliations:

[1]Department of Neuroscience, University of Virginia, Charlottesville, VA, USA

[2]Neuroscience Graduate Program, University of Virginia, Charlottesville, VA, USA

[3]Center for Brain Immunology and Glia, University of Virginia, Charlottesville, VA, USA

*Corresponding author. Email: ag7h@virginia.edu.

Abstract:

Multiple sclerosis (MS) is a T cell driven autoimmune disease that attacks the myelin of the central nervous system and currently has no cure. MS etiology is linked to both the gut flora and external environmental factors but this connection is not well understood. One immune system regulator responsive to non-pathogenic external stimuli is the aryl hydrocarbon receptor (AHR). The AHR, which binds diverse molecules present in the environment in barrier tissues, is a therapeutic target for MS. However, AHR's precise function in T lymphocytes, the orchestrators of MS, has not been described. Here we show that in a mouse model of MS, T cell specific *Ahr* knockout leads to recovery driven by a decrease in T cell fitness. At the mechanistic level, we demonstrate that the absence of AHR changes the gut microenvironment composition to generate metabolites that impact T cell viability, such as bile salts and short chain fatty acids. Our study demonstrates a newly emerging role for AHR in mediating the interdependence between T lymphocytes and the microbiota, while simultaneously identifying new potential molecular targets for the treatment of MS and other autoimmune diseases.

INTRODUCTION

Multiple sclerosis (MS) is a chronic inflammatory demyelinating disease that affects 2.3 million people worldwide. MS etiology and pathology are linked to both genetic and environmental factors[1]. A primary environmental factor impacting disease pathology lies with the gut microbiota[2–5]. Indeed, the connection between the microbiota and the immune system in autoimmune disorders such as MS is well established[6]. The gut flora, composed of bacteria, fungi, and viruses, aids food digestion and maintains pathogen control, but recent studies have also highlighted the integral role of the microbiome in modulation of the homeostatic immune state both locally and systemically[7]. Gut dysbiosis is a hallmark of disease in both patients with MS and in experimental animal models of MS[2,8–11]. The dysbiotic microbiome can cause earlier onset and increase disease severity in mice [10]. Furthermore, germ-free mice lacking a microbiome are resistant to experimental autoimmune encephalomyelitis (EAE), an animal model of MS[12]. These findings spurred the examination of various bacterial supplements in mouse models of MS, and numerous potential candidates have been identified[6,13]. However, the mechanism(s) of action is not well understood. The importance of the microbiome in MS is well described, but a better understanding of the cross-talk between the immune system and the microbiome is required to translate these findings to the clinic. Further, discoveries in the context of MS provide a foundation for understanding environmental factors impacting many other autoimmune disorders.

The aryl hydrocarbon receptor (AHR) is a prime candidate for understanding the microbiome-immune interface. The AHR is a cytoplasmic receptor that, when activated, traffics to the nucleus to execute downstream transcriptional programing[14]. While canonical immune sensors have been primarily characterized based on their response to pathogenic material, the

AHR is a homeostatic regulator that is activated by a variety of nonpathogenic exogenous ligands present in barrier tissues. These ligands include indoles[15], kynurenines[16], and other small molecules[17]. Downstream immune effects are dependent on the cell type and ligand. The AHR has also been directly tied to MS. AHR activation is the suspected mechanism by which the novel MS therapeutic, Laquinimod, acts[18,19]. It is thought that AHR activation by Laquinimod in antigen presenting cells reduces the ratio between inflammatory T cells and regulatory T cells (Treg). Microbiome changes have been identified in AHR null mice and in mice treated with a potent AHR agonist 2,3,7,8-tetrachlorodibenzo-p-dioxin (TCDD), further supporting the connection between AHR, the microbiome and MS [20–24]. While AHR activity in response to microbiome derived metabolites is well described, a gap of knowledge remains about the impact of AHR expression on the microbiota composition and function.

Here, we explore the role of AHR activity in CD4+ T cells using EAE. We have demonstrated that deleting *Ahr* from CD4+ T cells increases recovery in EAE in a microbiome-dependent manner. This improved recovery was the result of increased T cell apoptosis after activation in the central nervous system (CNS). While AHR deficiency did not grossly alter the composition of the microbiome, it significantly impacted the production of microbiome-mediated metabolites. In particular, AHR deficiency in T cells led to an increase in bile acids (BA) and a subset of short-chain fatty acids (SCFA) that ultimately impacted T cell viability. Our study aimed to understand how a microbiota response element can act in the inverse in the context of autoimmunity. This is the first demonstration, to our knowledge, of a role for AHR in T lymphocytes as a regulator of the microbiome activity that ultimately influences the outcome of CNS autoimmunity. Our discovery builds a foundation for further work that could lead to a

microbiome centric approach to dampen the overactive immune system in MS and related autoimmune disorders.

RESULTS

Separately housed **CD4+ specific *Ahr* knockout mice recover from active EAE:**

Given the emerging role of the microbiome and the well accepted contribution of T cells to MS pathology, AHR is ideally positioned to influence the pathology of CNS autoimmunity. Here we explored the role of AHR in CD4+ T cells in EAE. For this study, we used the previously validated *Cd4*^{cre}*Ahr*$^{fl/fl}$ and littermate control *Ahr*$^{fl/fl}$ mouse strains[25]. Cohoused adult littermate mice were immunized with myelin oligodendrocyte glycoprotein (MOG)$^{35\text{-}55}$ to induce active EAE. The cohoused mice showed no difference in EAE clinical score when *Ahr* expression was removed from CD4+ cells (**Figure 1A, Supplement 1A**; Females **Supplement 1B-C;** Males). Further, we observed no difference in myelin content in the spinal cord, as revealed by Luxol Fast Blue staining at the chronic phase of disease (**Figure 1B-C**). To assess the role of AHR driven microbiome changes in EAE, we separated mice by genotype at weaning (3 weeks) and induced EAE between 8 and 16 weeks of age. In this condition, while the time of onset and the peak clinical scores of EAE were not impacted, mice lacking *Ahr* expression in T cells presented with a significant recovery when compared to wild type animals (Females; **Figure 1D, Supplement 1D**). Furthermore, the change in recovery does not appear to be driven by sex as it was conserved in both sexes (Males; **Supplement 1E-F**). Supporting the clinical scores, the demyelination of the spinal cords was not different between the two groups at the peak of disease (day 16); however, we noted a significant increase in myelin staining at the chronic phase (day 31) in the *Cd4*^{cre}*Ahr*$^{fl/fl}$ animals when compared to the control (**Figures 1E-**

G). Together, these data indicate that the lack of *Ahr* expression in CD4+ cells promotes EAE recovery in a microbiome-dependent manner that can be reversed by cohousing.

Fig. 1. **Separately housed *Cd4^{cre}Ahr$^{fl/fl}$* recover from EAE with increased myelin staining at chronic phase.** (**A**) Clinical score of *Cd4^{cre}Ahr$^{fl/fl}$* and *Ahr$^{fl/fl}$* mice cohoused (Females; Representative plot includes n= 9 mice/group; total replicates of N=2 experiments). Spinal cords sections of *Cd4^{cre}Ahr$^{fl/fl}$* and *Ahr$^{fl/fl}$* were stained with Luxol Fast Blue and Hematoxylin/Eosin stain a day 31 post EAE induction (**B**) Representative images and (C) quantification of myelin stain. Images from four equally spaced spinal cord levels were averaged for each mouse. (n=5 mice/group; Unpaired T test p=0.0706) (**D**) Clinical score of *Cd4^{cre}Ahr$^{fl/fl}$* and *Ahr$^{fl/fl}$* littermate controls separated at weaning (3 weeks of age). (Females; Representative plot includes n=8-9 mice/group; total replicates of N=2 experiments; Mann-Whitney U Test on total scores reported in legend [p=0.0096] and on single days reported on plot) (**E**) Luxol Fast Blue with Hematoxylin/Eosin stain at the peak stage of EAE (day 16) and at chronic phase (day 31). (**F**) Quantification of myelin stain by Luxol Fast Blue alone in *Ahr$^{fl/fl}$* mice and (**G**) *Cd4^{cre}Ahr$^{fl/fl}$* mice. (n=7-8 mice/group; N=2 experiments; Unpaired T tests [p=0.8343, 0.0322]) Scale bars represent 400μm. Error bars represent standard error from the mean.

T cell differentiation and activity are unchanged in *Cd4^{cre}Ahr$^{fl/fl}$* mice:

CD4+ T cells are responsible for orchestrating EAE pathology, and defects in these cells have been shown to impact disease outcomes[26]. Additionally, AHR agonists can modulate T cell skewing in a ligand dependent manner *in vivo*[27]. We aimed to explore the role of AHR in T cells differentiation and cytokines production. First, we examined T cell differentiation and

the production of cytokines in cohoused *Cd4*^{cre}*Ahr*$^{fl/fl}$ mice. We found that the deletion of AHR in T cells did not impact their capacity for *in vitro* differentiation as determined by expression of lineage transcription factors by flow cytometry (**Figure 2A-E**) or production of the signature cytokine for each lineage by ELISA (**Figure 2F-I**). This was mirrored in separately housed animals (**Supplement 2A-G**). Furthermore, there were no differences in the immune cell composition between the knockout and control animals at baseline (**Figure 2J-M**). We next measured several cytokines important to EAE induction in the spinal cords of mice at the peak of disease. We expected to see significant reduction in the pathological cytokines in the separately housed *Cd4*^{cre}*Ahr*$^{fl/fl}$ mice that ultimately recover, but surprisingly we found minimal differences (**Figure 2N-S**). The only change was a small reduction in TNFα which may warrant further investigation. These findings suggest that CD4 cell intrinsic AHR activity is not necessary for normal T cell development and cytokines expression supporting published work indicating that AHR activation of the antigen presenting cell may be more important to T cell subset generation *in vivo*[28–30]. Further, these data reinforce the hypothesis that the T cell-intrinsic reduction of AHR activity in *Cd4*^{cre}*Ahr*$^{fl/fl}$ mice is not responsible for EAE recovery described in separately housed mice.

Fig. 2. *Ahr* knockout in CD4+ cells does not influence T cell differentiation. (**A**) Naïve CD4+ T cells were isolated from cohoused *Cd4*^{cre}*Ahr*$^{fl/fl}$ and littermate control animals and treated to promote differentiation. Flow cytometry gating strategy to measure percent of cells expressing the transcription factors specific to each cell type is shown. (**B**) Representative histogram and quantification of Tbet+ cells after *in vitro* differentiation of naïve CD4+ cells to T_H1 cell type, (n=6 mice/group; N=2 experiments;

Unpaired T test [p=0.8715]) (**C**) GATA3 staining of T_H2 differentiated cells, (n=6 mice/group; N=2 experiments; Unpaired T test [p=0.9356]), (**D**) RORγt staining of T_H17 cells (n=8 mice/group; N=3 experiments; Unpaired T test [p=0.3989]) (**E**), and FoxP3 staining for T_{regs}.(n=8 mice/group; N=3 experiments; Unpaired T test [p=0.4078]). (**F**) ELISA analysis of culture supernatant after 24 hours of anti-CD3 stimulation in $T_H1$cells (n=9 mice/group; N=3 experiments; Unpaired T test [p=0.3924]) (**G**) T_H2 cells(n=8 mice/group; N=3 experiments; Unpaired T test [p=0.5917]) (**H**) T_H17 cells (n=7-8 mice/group; N=3 experiments; Unpaired T test [p=0.4013]) (**I**) or Treg cells. (n=8 mice/group; N=3 experiments; Unpaired T test [p=0.2278]) (**J**) Gating strategy for (**K**) flow cytometry of single cell suspensions of Peyer's patches from cohoused *Cd4*^{cre}*Ahr*$^{fl/fl}$ and *Ahr*$^{fl/fl}$ mice. (Multiple T tests with Welch correction [p=0.070748, 0.081520, 0.325104, 0.080798]) (**L**) Analysis of cell compositions from mesenteric lymph nodes (Multiple T tests with Welch correction [p=0.127038, 0.179526, 0.444670, 0.118472]) (**M**) and the inguinal lymph nodes from cohoused *Cd4*^{cre}*Ahr*$^{fl/fl}$ and *Ahr*$^{fl/fl}$ mice (Multiple T tests with Welch correction [p=0.381964, 0.224164, 0.664161, 0.465348]) (**N-S**) Luminex assay on whole spinal cord homogenate of separately housed *Cd4*^{cre}*Ahr*$^{fl/fl}$ and *Ahr*$^{fl/fl}$ mice at the peak of disease (day 16 after immunization; n=8 mice/group; N=2 experiments; Unpaired T test) (N) [p=0.3087] (O) [p=0.4580] (P) [p=0.8313] (Q) [p=0.4941] (R) [p=0.0215] (S) [p=0.9333] Error bars represent standard error from the mean.

_Cd4_^{cre}_Ahr_$^{fl/fl}$ mice have fewer T cells in the spinal cord during EAE:

To determine whether EAE recovery in *Cd4*^{cre}*Ahr*$^{fl/fl}$ was linked to a difference in immune cell number during pathology, we quantified CD45+ immune cells in the spinal cord tissue using immunohistochemistry at the peak and chronic stages of EAE progression (**Figure 3A-B**). While the quantity of CD45+ cells was equivalent at the peak of the disease, we observed a decrease in the number of CD45+ cells in the *Cd4*^{cre}*Ahr*$^{fl/fl}$ spinal cord compared to controls at the chronic phase (**Figure 3B**). We next aimed to determine whether this reduction was a result of changes in the number of infiltrating T cells or macrophages. To accomplish this, we quantified expression of CD3, a pan-T cell marker, by immunohistochemistry. We saw no difference in the CD3+ cells in the spinal cord at the peak of disease (**Figure 3C**); however, at the chronic phase, significantly lower CD3+ T cell coverage was observed in the *Cd4*^{cre}*Ahr*$^{fl/fl}$ mice compared to the separately housed littermate controls (**Figure 3D**). Meanwhile, monocytes and macrophages, the other primary effector cells in EAE, showed no differences at either peak or chonic phase as shown by CD11b expression (**Figure 3E-F).** We confirmed this outcome using flow cytometry on percoll-isolated immune cells from the spinal cord. At the peak of disease, we again observed no differences in infiltrating T cells (CD4+ or CD8+), T cell subsets (RORgt+, Tbet+ GATA3+ or FoxP3+) or macrophages (CD11b+) (**Figure 3G-H**). At the chronic phase of disease, we found that the loss of T cells was limited to the CD4+ compartment and not the CD8+ compartment. Of the classic CD4 helper cell subtypes, all trended down in *Cd4*^{cre}*Ahr*$^{fl/fl}$ mice with no one subtype constituting a significant decrease, indicating a pan-CD4+ phenotype, not associated with a specific subtype of CD4+ T cells (**Figure 3F**). Taken together, our data suggest that in separately housed mice, EAE recovery observed in *Cd4*^{cre}*Ahr*$^{fl/fl}$ mice is not due to a difference in cytokine expression or T cell differentiation. Instead, recovery

correlates with an overall reduction in CD4+ T cell numbers at the chronic phase of disease and suggests an impact for AHR and the microbiome on CD4+ T cell fitness.

Fig. 3. Reduced CD3+ cells in the spinal cord of *Cd4^{cre}Ahr$^{fl/fl}$* mice correlate with clinical signs. (**A**) Spinal cords of separately housed *Cd4^{cre}Ahr$^{fl/fl}$* and *Ahr$^{fl/fl}$* littermate controls were stained for total immune cells (CD45+) by immunohistochemistry at four levels at the peak of disease (day 16 after immunization) (Each dot represents a mouse n=7 mice/group; N=2 experiments; Two-way ANOVA[p=0.5336]) (**B)** or at the chronic phase of disease (day 31 after immunization). (Two-way ANOVA [p=0.0419]; Sidak's multiple comparisons test [p=0.9896, 0.9209, 0.7898, 0.1753]) (**C**) Spinal cords of separately housed *Cd4^{cre}Ahr$^{fl/fl}$* and *Ahr$^{fl/fl}$* littermate controls were stained for T cells (CD3+) by immunohistochemistry at four levels at the peak of disease (day 16 after immunization) (n=7 mice/group; N=2 experiments, Two-way ANOVA [p=0.0830]) (**D**) or at chronic phase of disease (day 31 after immunization). (n=7 mice/group; N=2 experiments, Two-way ANOVA [p=0.0054]; Sidak's multiple comparisons test [p=0.9578, 0.9029, 0.7095, 0.0070]) (**E**) Spinal cords of separately housed *Cd4^{cre}Ahr$^{fl/fl}$* and *Ahr$^{fl/fl}$* littermate controls were stained for macrophages (CD11b+) by immunohistochemistry at four levels at the peak of disease (day 16 after immunization) (n=4-5 mice/group; N=2 experiments; Two-way ANOVA [p=0.1271]) (**F**) or at chronic phase of disease (day 31 after immunization). (n=5 mice/group; N=2 experiments, Two-way ANOVA [p=0.2269]) (**G**) Gating strategy for flow cytometry analysis of immune cells isolated from dissociated spinal cord tissue (**H**) at peak of disease (day 16 after immunization) (n=5-6/group; Multiple Unpaired T Tests

with Benjamini and Yekutieli corrections [p values listed in supplement]). (**I**) or chronic phase of disease (day 31 after immunization) (n=5 mice/group; Multiple Unpaired T Tests with Benjamini and Yekutieli corrections [p values listed in supplement]). Scale bars represent 400μm. Error bars represent standard error from the mean.

Apoptosis of *Ahr* deficient CD4 T cells is dependent on gut-derived small molecules:

We next investigated the mechanism behind the reduced T cell numbers in the spinal cords of $Cd4^{cre}$ $Ahr^{fl/fl}$ mice during chronic EAE. We performed a gene expression analysis on whole spinal cord tissues isolated from two $Cd4^{cre}Ahr^{fl/fl}$ and two $Ahr^{fl/fl}$ animals at the peak of EAE using a qPCR array composed of 384 genes associated with neuroinflammation. We found that the expression of many genes involved in apoptosis were modulated in the spinal cord tissue of $Cd4^{cre}Ahr^{fl/fl}$ mice; in particular we noted increased expression of *Fas, GrB, Casp3,* and *Casp9* and decreased expression of the antiapoptotic transcript of *Xiap*, indicating an increase in apoptosis in CD4 specific *Ahr*-deficient mice (**Supplement 3A-B**). To test if T cells lacking AHR were undergoing apoptosis in EAE, we stained spinal cords sections for CD3 expression by immunofluorescence and TUNEL assay (**Figure 4A**). While we could detect some apoptotic T cells in the spinal cords of control mice subjected to EAE, CD3+TUNEL+ cell numbers were significantly increased in the spinal cords of *Ahr* deficient animals (closed triangles; **Figure 4B**). We confirmed this observation by quantifying cellular death of isolated immune cells from the spinal cord at the peak of disease using flow cytometry. We observed a significant and specific increase in the percentage of dead CD4+ T cells without change in the percentage of dead CD8+ and or total TCRB+ cells between genotypes (**Figure 4C**). To further understand the mechanisms behind these observations, we focused examination on the primary pathogenic

subset of CD4+ cells in EAE, the type 17 T helper cell (T_H17)[31]. To obtain T_H17 cells we isolated naïve CD4+ cells from the lymph nodes and spleen, then cultured the cells in T_H17 differentiation conditions. Similar to the *in vivo* observations, *Cd4*^{cre}*Ahr*$^{fl/fl}$ T_H17 cells have a significant increase in apoptosis after mild *in vitro* stimulation by anti-CD3 as measured by Annexin V staining compared to littermate controls (**Figure 4D**). Increased T_H17 cell death was only observed in cells isolated from *Cd4*^{cre}*Ahr*$^{fl/fl}$ animals separated at weaning, as T cells isolated from cohoused *Cd4*^{cre}*Ahr*$^{fl/fl}$ mice did not display elevated apoptosis (**Figure 4E**). Taken together, these results support the hypothesis that gut microenvironment may be implicated in the *Ahr*-dependent T cell fitness phenotype. To directly test this hypothesis, we isolated metabolites (<3kDa) from cecums of separately housed *Cd4*^{cre}*Ahr*$^{fl/fl}$ and *Ahr*$^{fl/fl}$ mice, and added them to *in vitro* skewed T_H17 cells prepared from C57BL6/J mice during the 24 hour stimulation period. We next analyzed apoptosis by flow cytometry. T_H17 cells exposed to metabolites derived from the gut of *Cd4*^{cre}*Ahr*$^{fl/fl}$ mice had elevated apoptosis compared to cells exposed to metabolites from *Ahr*$^{fl/fl}$ microbiome (**Figure 4F**). Collectively, these data demonstrate that exposure to the microbial metabolites from *Cd4*^{cre}*Ahr*$^{fl/fl}$ mice is sufficient to induce early T cell apoptosis which likely contributes to recovery in EAE.

Fig 4. T cell apoptosis is increased in animals who recover from EAE. (**A**) Representative image of spinal cords stained with TUNEL assay and T cell marker at the peak of disease (CD3). Closed triangles indicate TUNEL+CD3+ cells and arrows indicate TUNEL+CD3- cells. Scale bar = 400µm. (**B**) Quantification of the number of TUNEL+ T cells (2-6 lesion sites averaged per animal; n=5-6 mice; N=2 EAE experiments; Unpaired T test [p=0.0357]). (**C**) T cells isolated from the spinal cord at the

peak of disease stained with viability dye and measured by flow cytometry. Cells gated on singlets, CD45+, gate shown on x-axis, then dead cells (n=5 mice/group; Two-way ANOVA [p=0.0192] with Sidak's Multiple Comparison Tests [p=0.0465, 0.2862, 0.6800]). (**D**) T cells skewed to T_H17 *in vitro* from separately housed *Cd4*^{cre}*Ahr*$^{fl/fl}$ mice stained for apoptotic marker Annexin V 24 hours after stimulation with anti-CD3 antibody. (n=6 mice/group; N=2 experiments; Unpaired T test [p=0.0133]). (**E**) T_H17 cells from cohoused *Cd4*^{cre}*Ahr*$^{fl/fl}$ and *Ahr*$^{fl/fl}$ mice show no differences in the number of Annexin V positive cells 24 hours after stimulation with anti-CD3 antibody. (n=5-6 mice/group; N=2 experiments; Unpaired T test [p=0.5851]). (**F**) *In vitro* differentiated T_H17 cells from C57BL6/J mice were exposed to the <3kDa fraction of cecal contents from *Ahr*$^{fl/fl}$ and *Cd4*^{cre}*Ahr*$^{fl/fl}$ mice for 24 hours with anti-CD3 stimulation. (n=6-9 mice/group; N=3 experiments; Mixed-effects analysis, with Geisser-Greenhouse correction [p=0.0013]; Tukey's post hoc analysis [Ctr v Fl p=0.7729; Ctr v Cre p=0.0333, Fl v Cre p<0.0001]). Error bars represent standard error from the mean.

Metabolomic differences in the gut microenvironment are evident in separately housed *Cd4*^{cre}*Ahr*$^{fl/fl}$ mice:

To identify the impact of CD4+ cell AHR loss on the gut microenvironment, we began by performing 16S sequencing of DNA isolated from fecal pellets and cecal contents of *Ahr*$^{fl/fl}$ or *Cd4*^{cre}*Ahr*$^{fl/fl}$ mice. Neither cohoused nor separately housed animals saw differences in fecal or cecal microbial signatures (**Supplement 4A-D**). Given the marked effect of the metabolites prepared from the cecums of *Cd4*^{cre}*Ahr*$^{fl/fl}$ and *Ahr*$^{fl/fl}$ on T cell apoptosis (**Figure 4F**), we next conducted untargeted metabolomics by LC-MS on these preparations (<3kDa). Two-dimensional

clustering of the annotated products revealed distinct clustering of genotypes, indicating different chemical profiles (**Figure 5A**). This difference occurred despite there being no significant difference in the 16S microbial signatures of the cecal contents suggesting that AHR activity in T cells modify microbial metabolism without altering the microbe composition to a degree that can be captured by 16S sequencing (**Supplement 4E-F**). Impact analysis of biological pathways identified primary bile acid biosynthesis as the most significantly upregulated pathway with six primary (cholic, taurocholic) or secondary (glycocholic, sulfocholic, dehydrocholic, lawsonic) bile acids significantly increased in the cecal microenvironment of *Cd4*^{cre}*Ahr*$^{fl/fl}$ mice (**Figure 5B, C**). Bile acids are dysregulated systemically in patients with MS and adding back primary bile acid is sufficient to reduce the severity of EAE[32]. Bile acid biosynthesis is known to be dependent on the gut microbiota composition[33,34]. Of the changed bile acids, taurocholic acid was the most highly upregulated with over a 10-fold increase in *Cd4*^{cre}*Ahr*$^{fl/fl}$ compared to control mice (**Figure 5C**). Increased bile acid accumulation in these mice may be due to the downregulation of bile acid transporters in the small intestine of the *Cd4*^{cre}*Ahr*$^{fl/fl}$ mice (**Figure 5D**). In addition to changes in bile acids, alanine, aspartate, and glutamate metabolism were also upregulated, whereas purine metabolism and tryptophan metabolism were downregulated in *Cd4*^{cre}*Ahr*$^{fl/fl}$ mice. As short chain fatty acids (SCFAs) have been reported to impact the viability of inflammatory T cell and cannot be captured through untargeted metabolomics, we next performed targeted SCFA metabolomics [35,36]. Isovaleric acid was the only SCFA with a significantly higher abundance in the *Cd4*^{cre}*Ahr*$^{fl/fl}$ cecums compared to controls (**Figure 5E**).

Fig 5. Elevated bile salts and SCFA detected in the cecum of AHR deficient mice. (**A**) Partial least-squares plot of LC-MS untargeted metabolomics of the <3kDa

fraction of the cecal contents from *Cd4*^{cre}*Ahr*$^{fl/fl}$ and *Ahr*$^{fl/fl}$ mice. (**B**) Metaboanalyst mouse KEGG pathways significantly changed by genotype. (**C**) MetaMapp network analysis visualizing the chemically or biologically related significantly changed molecules. (**D**) qPCR of bile acid transporters (*mrp3, ostb*) and bile acid response elements (*ezh2*, *fxr*) in bulk tissue of the duodenum and jejunum of separately housed animals illustrated as relative quantity (R.Q.) from *Ahr*$^{fl/fl}$ tissue . (n=6 mice/group; N=2 experiments; Multiple T Tests with Welch correction [duodenum p=0.0104, 0.3591, 0.0071, 0.3828; jejunum p=0.2230, 0.0623, 0.1487, 0.1004]). (**E**) Quantitative targeted metabolomics for short chain fatty acids show a significant increase in isovaleric acid, and a trending increase in valeric and hexanoic acid in *Cd4*^{cre}*Ahr*$^{fl/fl}$ mice. (n=6 mice/group; N=1 experiment; Unpaired T tests [p=0.0427, 0.1934, 0.1083]) Error bars represent standard error from the mean.

Taurocholic acid induces T_H17 cell apoptosis and protects from EAE:

The chemical composition of the cecal microenvironment between separately housed *Cd4*^{cre}*Ahr*$^{fl/fl}$ and *Ahr*$^{fl/fl}$ animals is significantly changed. We next aimed to determine what functional differences arose from the chemical differences both *in vitro* and *in vivo*. We first examined the most highly increased bile acid in *Cd4*^{cre}*Ahr*$^{fl/fl}$ mice, taurocholic acid. When administered to C57BL6/J derived T_H17 cells *in vitro*, taurocholic acid was sufficient to drive apoptosis similarly to cecal content isolates (**Figure 6A-B**). We also examined isovaleric acid, the short chain fatty acid, elevated in the absence of AHR. Similarly to taurocholic acid, isovaleric acid could induce apoptosis of *in vitro* generated T_H17 cells (**Figure 6C**). Similar results were obtained with hexanoic acid, which was also trending higher in *Cd4*^{cre}*Ahr*$^{fl/fl}$ mice (**Figure 6C**). Collectively, our data suggest that the combined effects of the cecal milieu of

Cd4^{cre}*Ahr*$^{fl/fl}$ mice could induce changes in T cell fitness, ultimately resulting in recovery from paralysis in EAE. As such, we aimed to determine whether this held true *in vivo* by conducting a fecal microenvironment transfer to C57BL/6 wildtype mice. The mice were given a cocktail of oral antibiotics for two weeks followed by a series of three oral gavages of the flushed contents of the intestinal tract from separately housed *Cd4*^{cre}*Ahr*$^{fl/fl}$ and *Ahr*$^{fl/fl}$ animals. During this time the animals were also cohoused with an untreated member of the respective genotype to promote lasting engraftment of the microbiome (**Figure 6D**). When these mice underwent EAE, the wildtype mice given FMT from *Cd4*^{cre}*Ahr*$^{fl/fl}$ animals had a similar, but less pronounced reduction in severity as the donor mice (**Figure 6E-F**). Because the FMT resulted in an intermediate phenotype, we next aimed to determine whether an individual component of the gut microenvironment could act as a therapeutic for EAE. As taurocholic acid was the most efficient driver of apoptosis *in vitro* (**Figure 6B**) we chose this as our prime candidate. We administered taurocholic acid orally for seven days after EAE induction (**Figure 6G**). Compared to mice given saline, those receiving taurocholic acid had decreased peak EAE scores (**Figure 6H**) and delayed onset (**Figure 6I**). These data are in support of recent work showing that bile acid receptor agonists and bile acid cocktails can reduce T cell activation and suppress EAE [37,38].

Fig 6. Gut Microenvironment and bile salts can drive EAE recovery and T cell apoptosis (**A**) Schematic representation of experiments in B and C. *In vitro* derived T_H17 cells from C57/BL6/J mice were treated with a metabolite in addition to mild anti-CD3 stimulation for 24 hours. (**B**) Taurocholic acid (10μM and 100μM) was administered during anti-CD3 stimulation and apoptosis of T_H17 cells isolated from C57BL6/J mice was measured using Annexin V staining by flow cytometry. (n=5-6 mice/group; N=2 experiments; Mixed effects analysis with Geisser-Greenhouse

correction [p=0.0070]; Dunnett's multiple comparison test [Veh vs 10μM p=0.8178, Veh vs 100μM p=0.0233]) (**C**) Administration of isovaleric acid and hexanoic acid (short chain fatty acids that are increased in mice that recover) are sufficient to drive apoptosis in T_H17 cells isolated from C57BL6/J mice. (n=8 mice/group; N=2 experiments; RM one-way ANOVA with the Geisser-Greenhouse correction[p=0.0399] Dunnett's multiple comparisons test [Veh vs 1mM Hexanoic p=0.0764, Veh vs 10mM Hexanoic p=0.0352, Veh vs 1mM Isovaleric p=0.0026, Veh vs 10mM Isovaleric p=0.0254]). (**D**) Schematic depicting approach to FMT. (**E**) EAE clinical scores of C57BL6/J mice receiving FMT from separately housed *Ahr*$^{fl/fl}$ or *Cd4*^{cre}*Ahr*$^{fl/fl}$ mice. (Females; Representative plot includes n=11 mice/group; total replicates of N=2 experiments; Mann-Whitney U Test on total scores reported in legend [p=0.0096]. (**F**) Incidence of clinical sign development in mice treated with FMT. (**G**) Schematic depicting approach to oral supplement of 12.5 mg taurocholic acid/day in C57BL6/J mice immunized for EAE. (**H**) EAE clinical scores of C57BL6/J mice receiving 7 days of oral taurocholic acid from separately housed *Ahr*$^{fl/fl}$ or *Cd4*^{cre}*Ahr*$^{fl/fl}$ mice. (Females; n=12 mice/group; total replicates of N=1 experiment; Mann-Whitney U Test on single days reported on plot). (**I**) Incidence of clinical sign development in mice treated with taurocholic acid. Error bars represent standard error from the mean.

DISCUSSION

Here we demonstrate that the deletion of the aryl hydrocarbon receptor (AHR) in CD4+ cells can promote recovery in chronic EAE while having no impact on the onset nor the initial magnitude of the disease. We further show that this phenotype is dependent on the microbiome, as cohousing littermate *Cd4*^{cre}*Ahr*$^{fl/fl}$ and *Ahr*$^{fl/fl}$ mice abrogates recovery in EAE. These data are

in support of previous work in similar models has shown no difference in EAE recovery after T cell-specific *Ahr* deletion [39]. At the mechanistic level, our data suggest that specific metabolites elevated in the cecum of $Cd4^{cre}Ahr^{fl/fl}$ mice reduce T cell fitness and viability. In particular, the cecal environment of $Cd4^{cre}Ahr^{fl/fl}$ animals is characterized by high levels of isovaleric acid and taurocholic acid, which induce T cell apoptosis *in vitro,* suggesting a potential mechanism for EAE recovery.

AHR activity can regulate autoimmunity via natural killer (NK) cells[40], macrophages[41], dendritic cells[42], and T cells[27,30,43]-all contributors to EAE pathogenesis. AHR activation is a known regulator of T cell differentiation and inflammatory to regulatory T cell ratios. Importantly, T cell activity is dependent on the specific ligand activation with some promoting a pro-inflammatory environment, and others having the opposite effect[27]. It has been postulated that T cell intrinsic AHR activity is necessary for differentiation but several groups have shown that AHR antagonists do not have a cell intrinsic effect on T cell differentiation leaving remaining questions in the field[44]. Here we demonstrate that T cell-specific AHR expression is not necessary for the differentiation of T cells *in vitro* supporting the hypothesis that the AHR activity in antigen presenting cell is the necessary factor influencing T cell differentiation *in vivo*[28–30]. Beyond T cells, AHR activation in glial cells regulates the pathogenic effects of microglia and astrocytes in EAE via changed cytokine production [45,46]. AHR's ubiquitous expression in barrier tissues coupled with its complex ligand binding profile warrants further study of AHR function in autoimmunity. We have identified that the changes of the luminal microenvironment of the intestine resulting from *Ahr* knockout in CD4+ cells lead to decreased post-activation lifespan in T cells; however, the impact of these changes on other cell types and other models of autoimmunity have yet to be

determined. Though we aimed to target T cells using the CD4 cre line, we acknowledge that other CD4 expressing cells including some gut macrophages may also be contributing to the observed phenotype.

Bile acids, SCFAs, and other small molecules we identified can move into circulation and some can gain entry into the central nervous system by crossing the blood brain barrier[47]. There are likely systemic effects that have yet to be described. For example, our data suggest that significant remyelination is taking place in the chronic phase of EAE in CD4 specific *Ahr* knockout animals. Given the described impact of the microbiome and SCFA on myelination [48,49], it would be critical to test if the metabolic signature generated by the lack of *Ahr* in T cells can influence oligodendrocyte generation.

The data presented here support a bidirectional communication between T cells and the microbiome via AHR. However, it remains to be understood how T cells can modulate the metabolic signature of the cecum. We hypothesize that there are many mechanisms that could be mediating the change. For example, we show that the expression on bile acid transporters are reduced in the intestines of mice with *Ahr* deletion. This could lead to heightened levels of bile acids which have an impact on microbial viability, metabolism, and community structure. Additionally, it is possible that *Ahr* deletion in T cells may lead to modulation of IgA secretion by B cells[50,51]. IgA is the primary mechanism by which the adaptive immune system can directly modulate mucosal microbial communities[50]. An alternative hypothesis is that immune cell activity is modulating antimicrobial peptide release indirectly through communication with Paneth cells[52,53]. Most work on these systems thus far has focused on models of severe microbiome dysbiosis. Less is known about the subtler changes in the microbiome subject to homeostatic regulation. Therefore, the mechanism by which the adaptive immune system can

interface with the microbiota is of great interest for understanding the basis of autoimmune disorders.

Ahr knockout in T cells results in a change in both primary and conjugated bile acids in the cecum. Bile acids are produced by the host for digestion and are normally reabsorbed by transporters (primary) or passively (primary conjugated) in the ileum while secondary bile acids are not as easily absorbed [54]. There is an increase in conjugated bile acids in *Ahr* knockout mice, but lower levels of secondary bile acids. This is the inverse of patients with MS indicating that there may be a causative connection in both patients and mice with EAE[32]. Further studies are needed to understand which step of this pathway: production, conversion or absorption are influenced by the gut flora and/or the T cells. Our results support the existing work in synthetic bile acid receptor agonists showing that T cell fitness and activity can be mediated by bile acid receptor activation[37,38]. As previous groups have shown that T cells traffic to the gut before the CNS during EAE, we hypothesize that exposure to these factors during priming in the lymph node may lead to the early apoptosis after trafficking to the CNS[55]. This evidence that bile acids can have a direct influence on T cell function warrants further study in the context of autoimmune diseases.

Microbiome-modulated immune responses become particularly important in patients with chronic and relapsing autoimmune conditions like MS[56–60]. We have described a novel function for the environmental sensor AHR in T cells as a regulator of the gut microenvironment. As we further understand the complexities of harnessing the gut microbiome, we predict tools for controlling host-derived microbe modulation will be a new frontier for therapeutics. Our work is an important step in the discovery of a targetable endogenous modulator of the microbiome opens a potential new therapeutic avenue for MS patients.

MATERIALS AND METHODS

Experimental Design: The objective of these studies was to understand the role of CD4 specific AHR activity in EAE. Immunophenotyping and characterization of the mice occurred in cohoused mice to determine the purely genetic differences. Once no major changes were discovered in the *Ahr* knockout mice, we began to separately house them based on genotype. This allowed us to examine the microbiome-dependent features of autoimmunity and the development of further hypotheses. Sample sizes were determined by power analysis. The final desired n was divided by two and included for each experiment. In this way, we have two independent experiments resulting in appropriate power. Except where otherwise stated, all experiments were conducted twice independently. Data collection for all EAE experiments ended at 30 days- the time point at which we have defined as chronic stage. All experiments were conducted on age- and sex- matched animals. Histological analysis was conducted by a blinded investigator. Clinical scores are reported as the average of two blinded investigators to account for interrater variability. Statistical outliers identified using the ROUT method (Q=1%) are not included in analysis or figures.

Mice: AHR$^{tm3.1Bra}$/J(Ahr^{fx}) (#006203), B6.Cg-Tg(Cd4-cre)1Cwi/BfluJ (CD4Cre) (#022071), and C57BL/6J (#000664) mice were purchased from Jackson Laboratories. Mice were bred in-house with a 12-hour light/dark schedule. Cohoused mice were housed with their littermates of the same sex from birth. Separately housed mice were separated at weaning (3 weeks) based on presence of Cre. Litters born within 4 days of each other were housed together to achieve 2-5 mice per cage. All procedures were approved by the University of Virginia ACUC (protocol #1918).

Experimental autoimmune encephalomyelitis: EAE was induced in both male and female mice between 8 and 12 weeks of age. MOG_{35-55} peptide (100μg, CSBio, CS0681) was emulsified in complete Freund's adjuvant containing *Mycobacterium tuberculosis* (1mg/mL, Sigma, F5881; M. tuberculosis (BD 231141) added to final concentration of 4mg/mL) and was injected subcutaneously (100 μL volume) at the base of the tail. Pertussis toxin (200 ng, List Biologicals, 180) was administered i.p. on the day of and 1 day after MOG immunization. Mice were scored daily by two blinded evaluators using the following scale: 0-no clinical disease, 1-limp tail, 2-hindlimb incoordination, 3-hindlimb weakness, 4-hindlimb paralysis, 5-moribund. As is standard practice, animals who did not develop any signs of EAE were excluded from analysis. Total incidence including excluded animals is reported in the supplement.

Immunohistochemistry and Fluorescent Microscopy: Spinal cords were prepared as previously described[61]. Slides were deparaffinized using xylenes and an ethanol gradient. IHC antibodies used were anti-CD3 (Dako; A0452) at 1:200 dilution and anti-CD45 (BD Biosciences; 550539) at 1:80 dilution. Adjacent sections were stained with Luxol Fast Blue and Hemtoxylin and Eosin for demyelinating plaques. In short, slides were deparaffinized using xylenes and an ethanol gradient. Slides were stained with Luxol Fast Blue at 56 ºC overnight. Slides were rinsed with distilled water and then 0.05% Lithium carbonate until sharp contrast between white matter and grey matter was evident. Slides were imaged using an EVOS microscope. All images were analyzed with ImageJ by setting a threshold in the negative control and evaluating percent positive area within the white matter of the spinal cord. Luxol Fast Blue alone was used for quantification of myelin coverage while Luxol Fast Blue with H&E images were used in the figure to highlight lesions. Histological analysis was performed by a blinded evaluator.

For TUNEL staining, cryosections (30μm) were stained with anti-CD3 (eBioscience; 50-0032-82) or isotype control (Fisher Scientific; 14-0032-82) as previously described[61]. A positive control slide was treated with DNAse (3000U/mL). After staining, sections were fixed with paraformaldehyde for 15 minutes at room temperature. Sections were washed two times in PBS followed by proteinase K (200ug/mL in PBS) treatment for 10 minutes at room temperature. Sections were washed twice with PBS and incubated with TUNEL reaction mixture (Roche; 12156792910) for 60 minutes at 37 ºC in a humidified chamber. Sections were washed three times in PBS and mounted using Prolong Gold Anti-Fade Reagent (Life Technologies). Slides were imaged with a Leica TCS SP8 confocal microscope. All images were analyzed with ImageJ. Histological analysis was performed by a blinded evaluator.

RNA Extraction and Quantitative PCR: Whole spinal cords or 0.5 cm sections of gut tissue were homogenized using a dounce homogenizer and RNA was extracted using the Bioline Isolate II RNA mini kit as per manufacture's protocol (BIO-52073). RNA was quantified with a Biotek Epoch Microplate Spectrophotometer. Normalized RNA was reverse transcribed to cDNA with the Bioline SensiFast cDNA Synthesis Kit (BIO-65054). For the qPCR array, two spinal cords per group were pooled and analyzed as described by the manufacturer (Demyelinating Diseases Tier 1-4 M384; 10038953). Primers for targeted qPCR are listed in the supplemental materials. Results were analyzed with the relative quantity (ΔΔCq) method.

Isolation and Preparation T cells: Mesenteric, inguinal, axial, and brachial lymph nodes plus the spleen were dissected from the mice after CO_2 euthanasia. They were then dissociated through sterile 70 μm filters and lysed with ACK lysis buffer (Quality Biological, 118-156-101). Naïve CD4+ T cells were then sorted using an EasySep Mouse CD4+ T cell Isolation Kit (Stem Cell Technologies, #19852). The cells were incubated at $1x10^6$ cells/mL in

skew media in anti-CD28 (InVivoMab, BE0015-5) and anti-CD3 (InVivoMab, BE0001-1) coated plates as previously described[62]. T_H1 and T_H2 media contained RPMI (Gibco, 11875-093) supplemented with 10% FBS (Optima, S12450H), 0.5% Pen/Strep (Gibco, 15240-062), 1mM sodium pyruvate (Gibco, 11360-070), 2mM L-glutamine (Gibco, 25030081), 10mM HEPES (Gibco, 15603-080), 1:100 NEAA (Gibco, 11140-050), and 50uM B-mercaptoethanol (Fisher Scientific, O3446I-100). Treg and T_H17 media contained IMDM (Gibco, 12440-053) using the same supplements. T_H1 skew media contained IL-2 (100U/mL; Tecin, 23-6019), IL-12 (10ng/mL; PeproTech, 210-12), and anti-IL-4 (10ug/mL; InVivoMab, BE0045). T_H2 skew media contained IL-2 (100U/mL; Tecin, 23-6019), IL-4 (10ng/mL; InVivoMab, BE0045), and anti-IFNγ (10ug/mL; InVivoMab BE0054). Treg skew media contained TGF-B (5ng/mL; BioLegend, 763102) and anti-CD28 (2ug/mL; InVivoMab, BE0015-5). T_H17 skew media contained IL-6 (20ng/mL; BioLegend, 575704), IL-23 (10ng/mL; Invitrogen, 14-8231), TGF-B (0.3ng/mL; BioLegend, 763102), anti-IL-4 (10ug/mL; InVivoMab, BE0045), and anti-IFNγ (10ug/mL; InVivoMab BE0054). T_H1 and T_H2 cell cultures were expanded on day 3 after plating by transferring cells to larger plates and adding 3x volume of RPMI supplemented media containing IL-2 (100U/mL). On day 5 skewing was complete and cells were washed and plated for downstream assays. Treg and T_H17 cell cultures were not expanded but simply washed and plated for downstream assays on day 4 after plating.

Apoptosis and Cytokines Production Assay: Skewed T cells were plated with respective treatments at $1x10^6$ cells/mL in 48 well plates coated with anti-CD3. After 24 hours, the supernatant was collected for ELISA assay or cells were collected for Annexin V staining. In short, cells were stained with Ghost Live Dead (Tonbo Biosciences; 13-0870), Annexin V (Fisher Scientific; BDB556420) per manufacturer's instructions (Annexin V, fixed using the

FoxP3 permeabilization, fixation kit (eBioscience; 00-5523-00), and stained with RORgt PE. Results were gated on singlets, RORgt+, and Annexin V+, L/D negative.

Enzyme-linked immunosorbent Assay: ELISA for IFNγ, IL-4, IL-17, and IL-10 were performed as previously described[63]. Antibodies used were as follows: anti-IFNγ (BioLegend; 517902), biotin labeled anti-INFγ (BioLegend; 505704), anti-IL-4 (Thermo Fisher; 14-7041-85), biotin labeled anti-IL-4 (Thermo Fisher; 13-7042-85), anti-IL-17 (eBioscience; 14-7175-85), biotin labeled anti-IL-17(eBioscience; 13-7177-85), anti-IL-10 (BioLegend; 505002), biotin labeled anti-IL-10 (BioLegend; 505004).

Isolation of Cecal Contents: For both metabolomics and *in vitro* analysis, the cecal contents were resuspended in 1mL of IMDM by vortexing. Preparations were then sequentially processed using first syringe filters to remove insoluble materials (70 μm, 40 μm, .22 μm) and then protein concentrators (50 and 3 kDa from Thermo Fischer scientific) to exclude macromolecules with a molecular weight > 3kDa. Preparations were used immediately, or flash frozen at -80C for up to 3 weeks.

Spinal Cord Dissociation Spinal cords were collected in 2.5 mL ice cold HBSS (Gibco, 14025134). Equal amounts of 4mg/mL collagenase 4 (Worthington; LS002139) with 50U/mL DNase (Worthington, LS002139) were added and samples were shaken three times at 37ºC for 15 minutes, triturating in between. Spinal cords were strained through a 70mm filter into 10mL DMEM (Gibco, 11965-092) with 10% FBS (R&D Systems; S12450H). The samples were then centrifuged at 260 g for 8 minutes. The pellet was resuspended in a 15mL tube in 12 mL of Percoll (GE Healthcare, 17-0891-01). The sample was then centrifuged at 650g for 25 min without brake. The myelin layer and supernatant were aspirated and the pellet was resuspended in 2mL of FACS buffer.

Spinal Cord Luminex Mice were perfused with PBS containing heparin (5U/mL; Sigma; H-3125) solution. Spinal cords were dissected and flash frozen. Frozen spinal cords were homogenized in 1mL of PBS with protease inhibitor (MedChem Express; HY-K0010) using a Dounce homogenizer. Triton X-100 was added to final concentration of 0.2% and samples were vortexed. Samples were centrifuged at 10,000g for 5 minutes at 4 °C and 200 µL was acquired from the top layer to be flash frozen for later analysis. Mouse T_H17 Luminex was run per manufacturer's instructions on a MagPix by the University of Virginia Flow Cytometry Core , RRID: SCR_017829.

Microbiome Transfer Female C57BL6/J mice were given drinking water containing 1g/L Ampicillin (Sigma-Aldrich; A8351-25G), 1g/L Neomycin (Sigma-Aldrich; N6386-25G), 1g/L Metronidazol (Sigma-Aldrich; M1547-25G), 500mg/mL Vancomycin (Sigma-Aldrich; V1130-5G), and 8mg/mL Splenda for two weeks. Mice were then orally gavaged with fresh filtered (40µm) cecal contents from pooled donor animals on day 0, day 2, and day 4 after removal from antibiotics. On the day of antibiotics withdrawal, a naïve microbiome donor animal was added to the cage and remained for the duration of the experiment. EAE was induced 2 weeks post reconstitution.

Bile Acid Supplement Female and male C57BL6/J mice were immunized with MOG as described above. Daily gavage of either 100µL of 125 mg/mL taurocholic acid (in saline) or 100µL of saline started on day 4 and continued through day 10. Mice were then monitored and scored as described earlier.

Flow Cytometry Single cell suspensions were incubated with Fc Block CD16/32 (Invitrogen, 14-0161-85). The cells were then incubated with a 1:200 dilution of antibody for surface stains and A Live/Dead Ghost Dye Violet 510 (Tonbo Biosciences; 13-0870). Surface

antibodies: 488-conjugated CD8 (Invitrogen; 53-008182), APCe780-conjugated TCRβ (Invitrogen; 47-5961-82), e450-conjugated CD4 (Invitrogen; 48-0042-820), 488 conjugated-CD11b (Invitrogen; 53-0112-82), and APC-conjugated CD45.2 (Biolegend; 109813). For transcription factor staining, the eBioscience FoxP3/Transcription Factor Staining Kit (00-5523-00) was used per manufacturer's instructions with intracellular antibodies: PE-conjugated RORγT (Invitrogen; 12-6981-82), PE-Cy7- conjugated FoxP3 (Invitrogen; 25-5773-82), PE-conjugated GATA3 (Invitrogen; 12-9966-42), PE-Cy7-conjugated Tbet (Biolegend; 644824). OneComp eBeads (Thermo Fisher Scientific, 01-111-42) were used for color controls. Flow cytometry was performed using a Beckman Coulter Gallios flow cytometer and data were analyzed with FlowJo software v10.7.1.

LC-MS Untargeted Metabolomics was performed by Creative Proteomics. Cecal samples (<3kDa) were prepared and concentrated as before as described before. Samples were thawed and lyophilized, 200μL of 80% methanol was added. Samples were vortexed and then sonicated for 30 minutes at 4 ºC. Samples were kept at -20 for 1 h, vortexed for 30s and kept at 4 ºC for 15min until they were centrifuged at 12000 rpm at 4 ºC for 15 min. 100μL of the supernatant and 2.5μL of DL-o-Chlorophenylalanine were used for LC-MS analysis. Separation is performed by Ultimate 3000 LC combined with Q Exactive MS (Thermo) and screened with ESI-MS. The LC system is comprised of ACQUITY UPLC HSS T3 (100×2.1mm×1.8 μm) with Ultimate 3000 LC. The mobile phase is composed of solvent A (0.05% formic acid water) and solvent B (acetonitrile) with a gradient elution (0-1.0 min, 5%B; 1.0-12.0 min, 5%-95%B; 12.0-13.5 min, 95%B; 13.5-13.6 min, 95%-5%B; 13.6-16.0 min, 5%B). The flow rate of the mobile phase is 0.3 mL·min-1. The column temperature is maintained at 40°C, and the sample manager temperature is set at 4°C. Mass spectrometry parameters in ESI+ and ESI- mode are listed as follows:

ESI+: Heater Temp 300 °C; Sheath Gas Flow rate, 45arb; Aux Gas Flow Rate, 15arb; Sweep Gas Flow Rate, 1arb; spray voltage, 3.0KV; Capillary Temp, 350 °C; S-Lens RF Level, 30%. ESI-: Heater Temp 300 °C, Sheath Gas Flow rate, 45arb; Aux Gas Flow Rate, 15arb; Sweep Gas Flow Rate, 1arb; spray voltage, 3.2KV; Capillary Temp,350 °C; S-Lens RF Level,60%.

LC-MS Data Processing LC-MS data was processed using R studio. Analysis was conducted using POMA Shiny version 1.4.0[64]. In short, we removed features with more than 20% missing values, normalized with log scaling and then completed sparse partial least squares discriminate analysis (sPLS-DA). Top ranked products were utilized in MetaMapp[65,66] analysis to produce a web of chemically and biologically related compounds. Finally, the top ranked products were also inputted into Metaboanalyst to complete pathway enrichment and determine mouse KEGG terms.

16S Sequencing Data Processing 16S Sequencing was conducted at Microbiome Insights (Cohoused Feces), ZymoBIOMICS (Separately Housed Cecum), and at the University of Virginia Genomics Core (Separately housed Feces). Initial sequence data was analyzed using the latest version of Quantitative Insights Into Microbial Ecology 2 (Qiime2 v2021.11)[67]. Demultiplexed paired-end sequence reads were preprocessed using DADA2[68]. The first 20 base pairs were trimmed from forward and reverse reads before they were merged to remove adaptors. Taxonomy was assigned to Amplicon Sequence Variants (ASVs) using a Naïve Bayes classifier trained on full length 16S sequences from the latest Greengenes16S database (13_8) clustered at 99% sequence similarity. Samples were rarified before core diversity analysis. Rarefied sampling depth was 16000 for cecal contents, 30000 for separately housed fecal contents, and 10,411 for cohoused fecal contents. Core diversity metrics were analyzed,

including number of ASVs. Nonmetric multidimensional scaling was performed in RStudio using the phyloseq package[69].

Statistical Analysis Unless otherwise noted, all statistical tests were run on Graph Pad Prism 9 Version 9.1.0. Statistical tests and p-values for each comparison are listed in the figure legends or in the supplementary report. In the figure legends, n denotes the total number of animals displayed in the figure used in analysis. In the figure legends, N denotes the total number of replicates that were completed for the given experiment. Testing level of α=0.05 was used throughout.

References and Notes

1. Compston A, Coles A. Multiple sclerosis. Vol. 372, The Lancet. Lancet; 2008. p. 1502–17.
2. Miyake S, Kim S, Suda W, Oshima K, Nakamura M, Matsuoka T, et al. Dysbiosis in the gut microbiota of patients with multiple sclerosis, with a striking depletion of species belonging to clostridia XIVa and IV clusters. PLoS One. 2015 Sep 14;10(9).
3. Aaen G, Belman A, Benson L, Casper C, Chitnis T, Gorman M, et al. Associations between the gut microbiota and host immune markers in pediatric multiple sclerosis and controls. BMC Neurol. 2016 Sep 21;16(1).
4. Chen J, Chia N, Kalari KR, Yao JZ, Novotna M, Soldan MMP, et al. Multiple sclerosis patients have a distinct gut microbiota compared to healthy controls. Sci Rep. 2016 Jun 27;6.
5. Jangi S, Gandhi R, Cox LM, Li N, Von Glehn F, Yan R, et al. Alterations of the human gut microbiome in multiple sclerosis. Nat Commun 2016 71. 2016 Jun 28;7(1):1–11.
6. Boziki MK, Kesidou E, Theotokis P, Mentis AFA, Karafoulidou E, Melnikov M, et al. Microbiome in multiple sclerosis; where are we, what we know and do not know. Vol. 10, Brain Sciences. MDPI AG; 2020.
7. Merchak A, Gaultier A. Microbial metabolites and immune regulation: New targets for major depressive disorder. Brain, Behav Immun - Heal. 2020 Nov 1;9:100169.
8. Levinthal DJ, Rahman A, Nusrat S, O'Leary M, Heyman R, Bielefeldt K. Adding to the Burden: Gastrointestinal Symptoms and Syndromes in Multiple Sclerosis. Mult Scler Int. 2013;2013:1–9.
9. Cox LM, Maghzi AH, Liu S, Tankou SK, Dhang FH, Willocq V, et al. Gut Microbiome in Progressive Multiple Sclerosis. Ann Neurol. 2021;89(6):1195–211.

10. Berer K, Gerdes LA, Cekanaviciute E, Jia X, Xiao L, Xia Z, et al. Gut microbiota from multiple sclerosis patients enables spontaneous autoimmune encephalomyelitis in mice. Proc Natl Acad Sci U S A. 2017 Oct 3;114(40):10719–24.

11. Jangi S, Gandhi R, Cox LM, Li N, Von Glehn F, Yan R, et al. Alterations of the human gut microbiome in multiple sclerosis. Nat Commun. 2016 Jun 28;7.

12. Berer K, Mues M, Koutrolos M, AlRasbi Z, Boziki M, Johner C, et al. Commensal microbiota and myelin autoantigen cooperate to trigger autoimmune demyelination. Nature. 2011 Nov 24;479(7374):538–41.

13. Johanson DM, Goertz JE, Marin IA, Costello J, Overall CC, Gaultier A. Experimental autoimmune encephalomyelitis is associated with changes of the microbiota composition in the gastrointestinal tract. Sci Rep. 2020 Dec 1;10(1).

14. Barroso A, Mahler JV, Fonseca-Castro PH, Quintana FJ. The aryl hydrocarbon receptor and the gut-brain axis. Cell Mol Immunol. 2021;18:259–68.

15. Hubbard TD, Murray IA, Bisson WH, Lahoti TS, Gowda K, Amin SG, et al. Adaptation of the human aryl hydrocarbon receptor to sense microbiota-derived indoles. Sci Rep. 2015;5.

16. Jin UH, Lee SO, Sridharan G, Lee K, Davidson LA, Jayaraman A, et al. Microbiome-Derived Tryptophan Metabolites and Their Aryl Hydrocarbon Receptor-Dependent Agonist and Antagonist Activities. Mol Pharmacol. 2014;85(5).

17. Denison MS, Faber SC. And now for something completely different: Diversity in ligand-dependent activation of Ah receptor responses. Vol. 2, Current Opinion in Toxicology. 2017.

18. Ott M, Avendanõ-Guzmán E, Ullrich E, Dreyer C, Strauss J, Harden M, et al. Laquinimod, a prototypic quinoline-3-carboxamide and aryl hydrocarbon receptor agonist, utilizes a CD155-mediated natural killer/dendritic cell interaction to suppress CNS autoimmunity. J Neuroinflammation. 2019 Feb 26;16(1):1–14.

19. Kaye J, Piryatinsky V, Birnberg T, Hingaly T, Raymond E, Kashi R, et al. Laquinimod arrests experimental autoimmune encephalomyelitis by activating the aryl hydrocarbon receptor. Proc Natl Acad Sci U S A. 2016 Oct 11;113(41):E6145–52.

20. Korecka A, Dona A, Lahiri S, Tett AJ, Al-Asmakh M, Braniste V, et al. Bidirectional communication between the Aryl hydrocarbon Receptor (AhR) and the microbiome tunes host metabolism. npj Biofilms Microbiomes 2016 21. 2016 Aug 24;2(1):1–10.

21. Yang F, DeLuca JAA, Menon R, Garcia-Vilarato E, Callaway E, Landrock KK, et al. Effect of diet and intestinal AhR expression on fecal microbiome and metabolomic profiles. Microb Cell Fact. 2020 Dec 1;19(1):1–18.

22. Murray IA, Nichols RG, Zhang L, Patterson AD, Perdew GH. Expression of the aryl hydrocarbon receptor contributes to the establishment of intestinal microbial community structure in mice. Sci Rep. 2016;6.

23. Fling RR, Zacharewski TR. Aryl hydrocarbon receptor (Ahr) activation by 2,3,7,8-tetrachlorodibenzo-p-dioxin (tcdd) dose-dependently shifts the gut microbiome consistent with the progression of non-alcoholic fatty liver disease. Int J Mol Sci. 2021 Nov

1;22(22).

24. Abdulla OA, Neamah W, Sultan M, Alghetaa HK, Singh N, Busbee PB, et al. The Ability of AhR Ligands to Attenuate Delayed Type Hypersensitivity Reaction Is Associated With Alterations in the Gut Microbiota. Front Immunol. 2021 Jun 29;12:2505.

25. Rivet-Noor CR, Merchak AR, Li S, Beiter RM, Lee S, Thomas JA, et al. Stress-induced despair behavior develops independently of the Ahr-RORγt axis in CD4□+□cells. Sci Reports 2022 121. 2022 May 21;12(1):1–10.

26. Kurschus FC. T cell mediated pathogenesis in EAE: Molecular mechanisms. Biomed J. 2015 May 1;38(3):183–93.

27. Ehrlich AK, Pennington JM, Bisson WH, Kolluri SK, Kerkvliet NI. TCDD, FICZ, and Other High Affinity AhR Ligands Dose-Dependently Determine the Fate of CD4+ T Cell Differentiation. Toxicol Sci. 2018;161(2):310–20.

28. Hong CH, Lin SH, Clausen BE, Lee CH. Selective AhR knockout in langerin-expressing cells abates Langerhans cells and polarizes Th2/Tr1 in epicutaneous protein sensitization. Proc Natl Acad Sci U S A. 2020 Jun 9;117(23):12980–90.

29. Duarte JH, Di Meglio P, Hirota K, Ahlfors H, Stockinger B. Differential Influences of the Aryl Hydrocarbon Receptor on Th17 Mediated Responses in vitro and in vivo. PLoS One. 2013 Nov 14;8(11):e79819.

30. Quintana FJ, Murugaiyan G, Farez MF, Mitsdoerffer M, Tukpah AM, Burns EJ, et al. An endogenous aryl hydrocarbon receptor ligand acts on dendritic cells and T cells to suppress experimental autoimmune encephalomyelitis. Proc Natl Acad Sci U S A. 2010 Nov 30;107(48):20768–73.

31. Angelou CC, Wells AC, Vijayaraghavan J, Dougan CE, Lawlor R, Iverson E, et al. Differentiation of Pathogenic Th17 Cells Is Negatively Regulated by Let-7 MicroRNAs in a Mouse Model of Multiple Sclerosis. Front Immunol. 2020 Jan 17;10:3125.

32. Bhargava P, Smith MD, Mische L, Harrington E, Fitzgerald KC, Martin K, et al. Bile acid metabolism is altered in multiple sclerosis and supplementation ameliorates neuroinflammation. J Clin Invest. 2020 Jul 1;130(7):3467.

33. Sayin SI, Wahlström A, Felin J, Jäntti S, Marschall HU, Bamberg K, et al. Gut microbiota regulates bile acid metabolism by reducing the levels of tauro-beta-muricholic acid, a naturally occurring FXR antagonist. Cell Metab. 2013 Feb 5;17(2):225–35.

34. Ma C, Han M, Heinrich B, Fu Q, Zhang Q, Sandhu M, et al. Gut microbiome–mediated bile acid metabolism regulates liver cancer via NKT cells. Science (80-). 2018 May 25;360(6391).

35. MA Z, N S, PM M, M T, V G, JL W, et al. Butyrate suppresses colonic inflammation through HDAC1-dependent Fas upregulation and Fas-mediated apoptosis of T cells. Am J Physiol Gastrointest Liver Physiol. 2012 Jun 15;302(12).

36. Kurita-Ochiai T, Ochiai K, Fukushima K. Butyric Acid-Induced T-Cell Apoptosis Is Mediated by Caspase-8 and -9 Activation in a Fas-Independent Manner. Clin Diagn Lab Immunol. 2001;8(2):325.

37. Lewis ND, Patnaude LA, Pelletier J, Souza DJ, Lukas SM, King FJ, et al. A GPBAR1 (TGR5) Small Molecule Agonist Shows Specific Inhibitory Effects on Myeloid Cell Activation In Vitro and Reduces Experimental Autoimmune Encephalitis (EAE) In Vivo. PLoS One. 2014 Jun 26;9(6):e100883.

38. Ho PP, Steinman L. Obeticholic acid, a synthetic bile acid agonist of the farnesoid X receptor, attenuates experimental autoimmune encephalomyelitis. Proc Natl Acad Sci U S A. 2016 Feb 9;113(6):1600.

39. Duarte JH, Di Meglio P, Hirota K, Ahlfors H, Stockinger B. Differential Influences of the Aryl Hydrocarbon Receptor on Th17 Mediated Responses in vitro and in vivo. 2013;8(11):e79819.

40. Shin JH, Moreno-Nieves UY, Zhang LH, Chen C, Dixon AL, Linde MH, et al. AHR Regulates NK Cell Migration via ASB2–Mediated Ubiquitination of Filamin A. Front Immunol. 2021 Feb 24;12:94.

41. Wang C, Ye Z, Kijlstra A, Zhou Y, Yang P. Activation of the aryl hydrocarbon receptor affects activation and function of human monocyte-derived dendritic cells. Clin Exp Immunol. 2014 Aug 1;177(2):521–30.

42. Quintana FJ, Murugaiyan G, Farez MF, Mitsdoerffer M, Tukpah AM, Burns EJ, et al. An endogenous aryl hydrocarbon receptor ligand acts on dendritic cells and T cells to suppress experimental autoimmune encephalomyelitis. Proc Natl Acad Sci U S A. 2010;107(48):20768–73.

43. Lee Y, Awasthi A, Yosef N, Quintana FJ, Xiao S, Peters A, et al. Induction and molecular signature of pathogenic T H 17 cells. Nat Immunol. 2012;

44. McAleer JP, Fan J, Roar B, Primerano DA, Denvir J. Cytokine Regulation in Human CD4 T Cells by the Aryl Hydrocarbon Receptor and Gq-Coupled Receptors. Sci Reports 2018 81. 2018 Jul 19;8(1):1–12.

45. Rothhammer V, Borucki DM, Tjon EC, Takenaka MC, Chao CC, Ardura-Fabregat A, et al. Microglial control of astrocytes in response to microbial metabolites. Nature. 2018;557:724–8.

46. Rothhammer V, Mascanfroni ID, Bunse L, Takenaka MC, Kenison JE, Mayo L, et al. Type i interferons and microbial metabolites of tryptophan modulate astrocyte activity and central nervous system inflammation via the aryl hydrocarbon receptor. Nat Med. 2016;22(6).

47. Parker A, Fonseca S, Carding SR. Gut microbes and metabolites as modulators of blood-brain barrier integrity and brain health. Gut Microbes. 2020 Mar 3;11(2):135.

48. Keogh CE, Kim DHJ, Pusceddu MM, Knotts TA, Rabasa G, Sladek JA, et al. Myelin as a regulator of development of the microbiota-gut-brain axis. Brain Behav Immun. 2021 Jan 1;91:437–50.

49. Hoban AE, Stilling RM, Ryan FJ, Shanahan F, Dinan TG, Claesson MJ, et al. Regulation of prefrontal cortex myelination by the microbiota. Transl Psychiatry. 2016 Apr 5;6(4).

50. Lycke NY, Bemark M. The regulation of gut mucosal IgA B-cell responses: recent developments. Mucosal Immunol 2017 106. 2017 Jul 26;10(6):1361–74.

51. Vaidyanathan B, Chaudhry A, Yewdell WT, Angeletti D, Yen WF, Wheatley AK, et al. The aryl hydrocarbon receptor controls cell-fate decisions in B cells. J Exp Med. 2017;214(1):197.

52. Araujo A, Safronova A, Burger E, López-Yglesias A, Giri S, Camanzo ET, et al. Ifn-g mediates paneth cell death via suppression of mtor. Elife. 2021 Oct 1;10.

53. Kamioka M, Goto Y, Nakamura K, Yokoi Y, Sugimoto R, Ohira S, et al. Intestinal commensal microbiota and cytokines regulate Fut2+ Paneth cells for gut defense. Proc Natl Acad Sci U S A. 2022 Jan 18;119(3).

54. Šarenac TM, Mikov M. Bile acid synthesis: From nature to the chemical modification and synthesis and their applications as drugs and nutrients. Front Pharmacol. 2018 Sep 25;9(SEP):939.

55. Duc D, Vigne S, Bernier-Latmani J, Yersin Y, Ruiz F, Gaïa N, et al. Disrupting Myelin-Specific Th17 Cell Gut Homing Confers Protection in an Adoptive Transfer Experimental Autoimmune Encephalomyelitis. Cell Rep. 2019 Oct 8;29(2):378-390.e4.

56. JG B, MV T, NL D, S O, JA S, E G, et al. Regulation of autoimmune myocarditis by host responses to the microbiome. Exp Mol Pathol. 2017 Oct 1;103(2):141–52.

57. Bergot AS, Giri R, Thomas R. The microbiome and rheumatoid arthritis. Best Pract Res Clin Rheumatol. 2019;33(6).

58. KL G, BP A, EMM Q. The microbiome and inflammatory bowel disease. J Allergy Clin Immunol. 2020 Jan 1;145(1):16–27.

59. J OR, TO K, LH K. The Gut Microbiome and Multiple Sclerosis. Cold Spring Harb Perspect Med. 2018 Jun 1;8(6).

60. YJ H, HA B. The microbiome in asthma. J Allergy Clin Immunol. 2015 Jan 1;135(1):25–30.

61. Chuang TY, Guo Y, Seki SM, Rosen AM, Johanson DM, Mandell JW, et al. LRP1 expression in microglia is protective during CNS autoimmunity. Acta Neuropathol Commun. 2016 Jul 11;4(1):68.

62. Seki SM, Stevenson M, Rosen AM, Arandjelovic S, Gemta L, Bullock TNJ, et al. Lineage-Specific Metabolic Properties and Vulnerabilities of T Cells in the Demyelinating Central Nervous System. J Immunol. 2017 Jun 15;198(12):4607–17.

63. Remick DG, Bolgos GR, Siddiqui J, Shin J, Nemzek JA. Six at six: interleukin-6 measured 6 h after the initiation of sepsis predicts mortality over 3 days. Shock. 2002;17(6):463–7.

64. Castellano-Escuder P, Andrés-Lacueva C, Sánchez-Pla A. POMA: User-friendly Workflow for Metabolomics and Proteomics Data Analysis. PLoS Comput Biol. 2021;17(7):e1009148.

65. Hartman AL, Lough DM, Barupal DK, Fiehn O, Fishbein T, Zasloff M, et al. Human gut microbiome adopts an alternative state following small bowel transplantation. Proc Natl Acad Sci U S A. 2009 Oct 6;106(40):17187–92.

66. Barupal DK, Haldiya PK, Wohlgemuth G, Kind T, Kothari SL, Pinkerton KE, et al.

MetaMapp: mapping and visualizing metabolomic data by integrating information from biochemical pathways and chemical and mass spectral similarity. BMC Bioinformatics. 2012 May 16;13(1):1–15.

67. Bolyen E, Rideout JR, Dillon MR, Bokulich NA, Abnet CC, Al-Ghalith GA, et al. Reproducible, interactive, scalable and extensible microbiome data science using QIIME 2. Nat Biotechnol 2019 378. 2019 Jul 24;37(8):852–7.

68. Callahan BJ, McMurdie PJ, Rosen MJ, Han AW, Johnson AJA, Holmes SP. DADA2: High-resolution sample inference from Illumina amplicon data. Nat Methods 2016 137. 2016 May 23;13(7):581–3.

69. McMurdie PJ, Holmes S. phyloseq: An R Package for Reproducible Interactive Analysis and Graphics of Microbiome Census Data. PLoS One. 2013 Apr 22;8(4):e61217.

Supplementary Materials

Figure S1. Separately housed *Cd4^{cre}Ahr$^{fl/fl}$* recover from EAE phase. (A) No genotype differences in EAE incidence from the experiment shown in Figure 1A. (B) No differences in EAE clinical score or (C) incidence in cohoused male mice (Males; n= 7-8; N=1; Mann-Whitney U Test [p=0.5680]) (A) No genotype differences in EAE incidence from the experiment shown in Figure 1D. (B) Separately housed male *Cd4^{cre}Ahr$^{fl/fl}$* mice recover from EAE while *Ahr$^{fl/fl}$* mice maintain paralysis. (Males; n=7-8/group; N=1; Mann-Whitney U Test on total scores reported in legend [p=0.0010] and on single days reported on plot) (C) No difference in incidence of cohoused male mice.

Figure S2. Lack of AHR in T cells isolated from separately housed mice does not impact differentiation capacity or cytokine production. Naïve T cells were isolated from separately housed at weaning animals and differentiated toward T_H1, T_H2, T_H17 and T_{reg} *in vitro*. Transcription factors expression was quantified by Flow Cytometry. (**A**) Quantification of Tbet+ cells differentiated to T_H1 cell type and stimulated for 24 hours with either anti-CD3 or anti-

CD28 (n=4 mice/group; N=1 experiment; Ordinary one-way ANOVA [p=0.2927]). (**B**) Quantification of GATA3+ cells differentiated to T_H2 cell type and stimulated for 24 hours with either anti-CD3 or anti-CD28 (n=4 mice/group; N=1 experiment; Ordinary one-way ANOVA [p=0.0076] followed by Tukey's Post-Hoc). (**C**) Quantification of RORγt+ cells differentiated to T_H17 cell type and stimulated for 24 hours with either anti-CD3 or anti-CD28 (n=4 mice/group; N=1 experiment; Ordinary one-way ANOVA [p=0.0163] followed by Tukey's Post-Hoc). (**D**) Quantification of FoxP3+ cells differentiated to T_{reg} cell type and stimulated for 24 hours with either anti-CD3 or anti-CD28 (n=4 mice/group; N=1 experiment; Ordinary one-way ANOVA [p=0.8801]). (**E**) IFNγ ELISA on supernatant of differentiated T_H1 cells stimulated for 24 hours with either anti-CD3 or anti-CD28 (n=4 mice/group; N=1 experiment; Ordinary one-way ANOVA [p=0.8639]). (**F**) IL-4 ELISA on supernatant of differentiated T_H2 cells stimulated for 24 hours with either anti-CD3 or anti-CD28 (n=4 mice/group; N=1 experiment; Ordinary one-way ANOVA [p=0.0064] followed by Tukey's Post-Hoc). (**G**) IL-17a ELISA on supernatant of differentiated T_H17 cells stimulated for 24 hours with either anti-CD3 or anti-CD28 (n=4 mice/group; N=1 experiment; Ordinary one-way ANOVA [p=0.4826]).

Figure S3. Higher apoptosis in CD4 T cells lacking AHR. (**A**) Gene expression analysis (qPCR array) performed on spinal cord RNAs prepared from separately housed *Cd4*^{cre}*Ahr*$^{fl/fl}$ mice and *Ahr*$^{fl/fl}$ littermate controls at the peak of disease (Day 16) shows increased pro-apoptotic transcripts and decreased anti-apoptotic transcript (cDNA prepared from 2 spinal cords were pooled for each sample). (**B**) Gating strategy for Annexin V+ apoptotic and necrotic cells shown in show in Figure 4 and S3C-D. (**C**) Quantification of total dead cells in separately housed T_H17 differentiated cells (n=3 mice/group; N=1 experiment; Unpaired T Test [p=0.5130]). (**D**) T cells differentiated to T_H1, T_H2, or T_{reg} *in vitro* from separately housed *Cd4*^{cre}*Ahr*$^{fl/fl}$ mice have higher

expression of the apoptotic marker Annexin V after 24 hours of CD3 stimulation. (n=3/group; N=1 experiment; Unpaired T tests [p=0.4276, 0.0078, 0.0442]).

Figure S4. Only subtle microbiota population changes in *Cd4^{cre}Ahr$^{fl/fl}$* mice (**A**) PCA plot and (**B**) microbiome composition at the genus level obtained from 16S sequencing performed on feces collected from cohoused animals. (Males; n=6/group) (**C**) PCA plot and (**D**) microbiome composition at the genus level obtained from 16S sequencing performed on feces collected from separately housed animals. (Males and Females; n= 10/group) (**E**) PCA plot and (**F**) microbiome composition at the genus level obtained from 16S sequencing performed on cecum collected from separately housed animals. (Males and Females; n=12/group)

Data S1. Statistical report for all data presented in the manuscript.

Data S2. Raw Data files from Negative ion mode LC-MS corresponding to Figure 5 A-C.

Data S3. Raw Data files from Positive ion mode LC-MS corresponding to Figure 5 A-C.

DECLARATION:

Ethics approval and consent to participate:

Not applicable.

Consent for publication:

Not applicable.

Availability of data and materials:

The datasets supporting the conclusions of this article are available in the NCBI Gene Expression Omnibus repository accession number GSE200440 and in additional files.
https://www.ncbi.nlm.nih.gov/geo/query/acc.cgi?acc=GSE200440

Competing interests:

Authors declare that they have no competing interests.
All authors have read and approved the manuscript.

Funding:

This work received funding from the National Institutes of Health (R33 MH108156 to A.G., T32 NS115657 to A.R.M., T32 GM008136 to R.M.B.), from the UVA Wagner fellowship (R.M.B.), from the Owens Family Foundation (A.G.) from the UVA Trans University Microbiome Initiative pilot grant (A.G. and A.R.M.) and from the UVA Presidential Fellowship in Neuroscience (C.R.N.).

Author contributions:

All authors have read and approved the manuscript

Conceptualization: ARM, AG
Methodology: ARM, AG
Investigation: ARM, HJC, LCB, RMB, CRN, RMB, ERS
Data Curation: DGO
Formal Analysis: ARM, DGO
Supervision: AG
Visualization: ARM
Writing—original draft: ARM, AG
Writing—review & editing: HJC, LCB, RMB, CRN, RMB, DGO
Funding Acquisition: AG

Acknowledgments:

The authors wish to thank the University of Virginia Biorepository and Tissue Research facility for their support with immunohistochemistry.
The authors would also like to thank Tula Raghavan, Dr. Sanja Arandjelovic, and Dr. Sharon Walsh for critical reading and members the University of Virginia Brain Immunology and Glia Center for scientific input.

Authors information:

Department of Neuroscience, University of Virginia, Charlottesville, VA, USA:

Andrea R. Merchak, Hannah J. Cahill, Lucille C. Brown, Ryan M. Brown, Courtney Rivet-Noor, Rebecca M. Beiter, Erica R. Slogar, Deniz G. Olgun, and Alban Gaultier

Neuroscience Graduate Program, University of Virginia, Charlottesville, VA, USA:

Andrea R. Merchak, Ryan M. Brown, Courtney Rivet-Noor, Rebecca M. Beiter and Alban Gaultier

Center for Brain Immunology and Glia, University of Virginia, Charlottesville, VA, USA:

Andrea R. Merchak, Ryan M. Brown, Courtney Rivet-Noor, Rebecca M. Beiter and Alban Gaultier

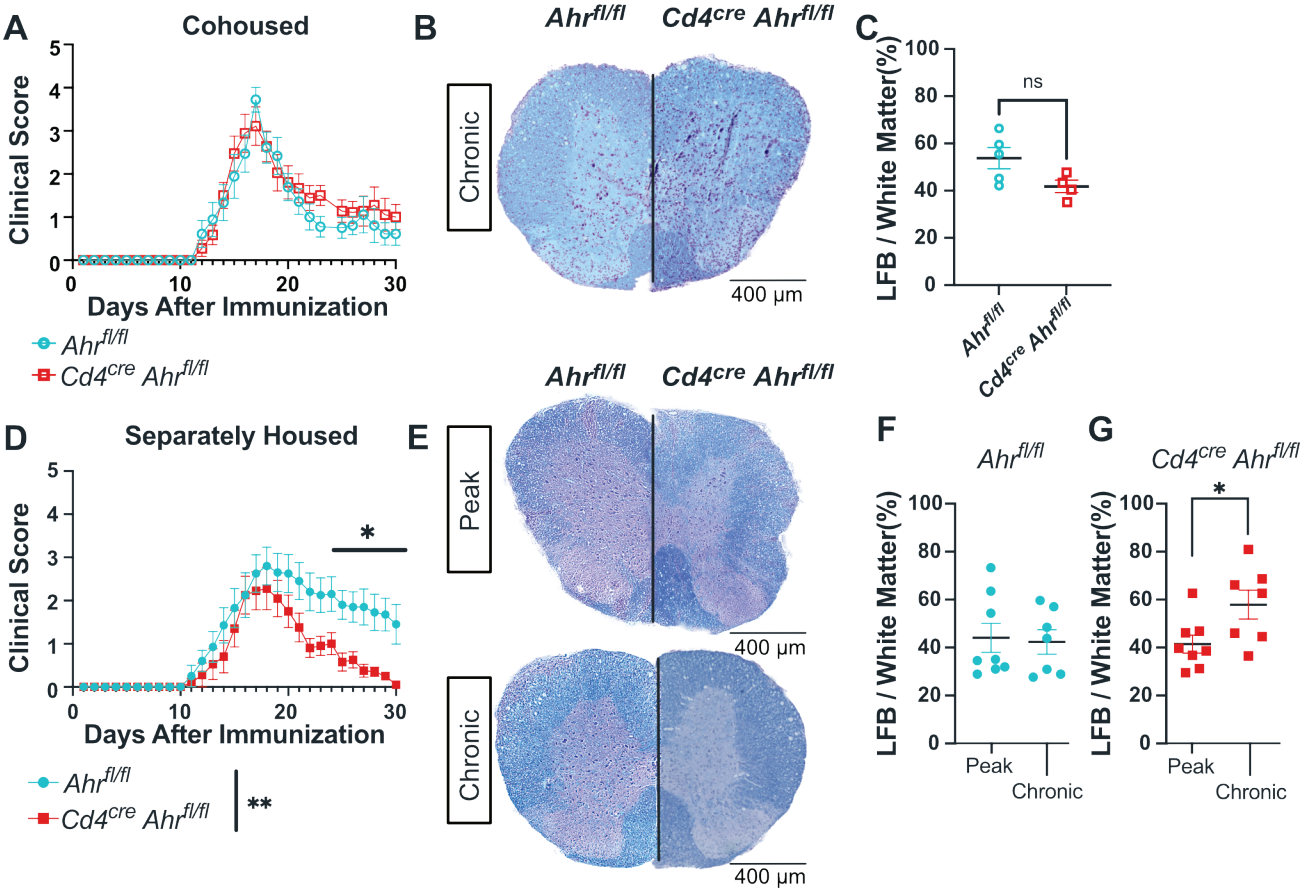
A
Cohoused
Clinical Score
Days After Immunization
Ahr fl/fl
Cd4cre Ahr fl/fl
B
Ahr fl/fl
Cd4cre Ahr fl/fl
Chronic
400 µm
C
LFB / White Matter(%)
ns
Ahr fl/fl
Cd4cre Ahr fl/fl
D
Separately Housed
Clinical Score
Days After Immunization
*
**
Ahr fl/fl
Cd4cre Ahr fl/fl
E
Ahr fl/fl
Cd4cre Ahr fl/fl
Peak
Chronic
400 µm
400 µm
F
Ahr fl/fl
LFB / White Matter(%)
Peak
Chronic
G
Cd4cre Ahr fl/fl
LFB / White Matter(%)
*
Peak
Chronic

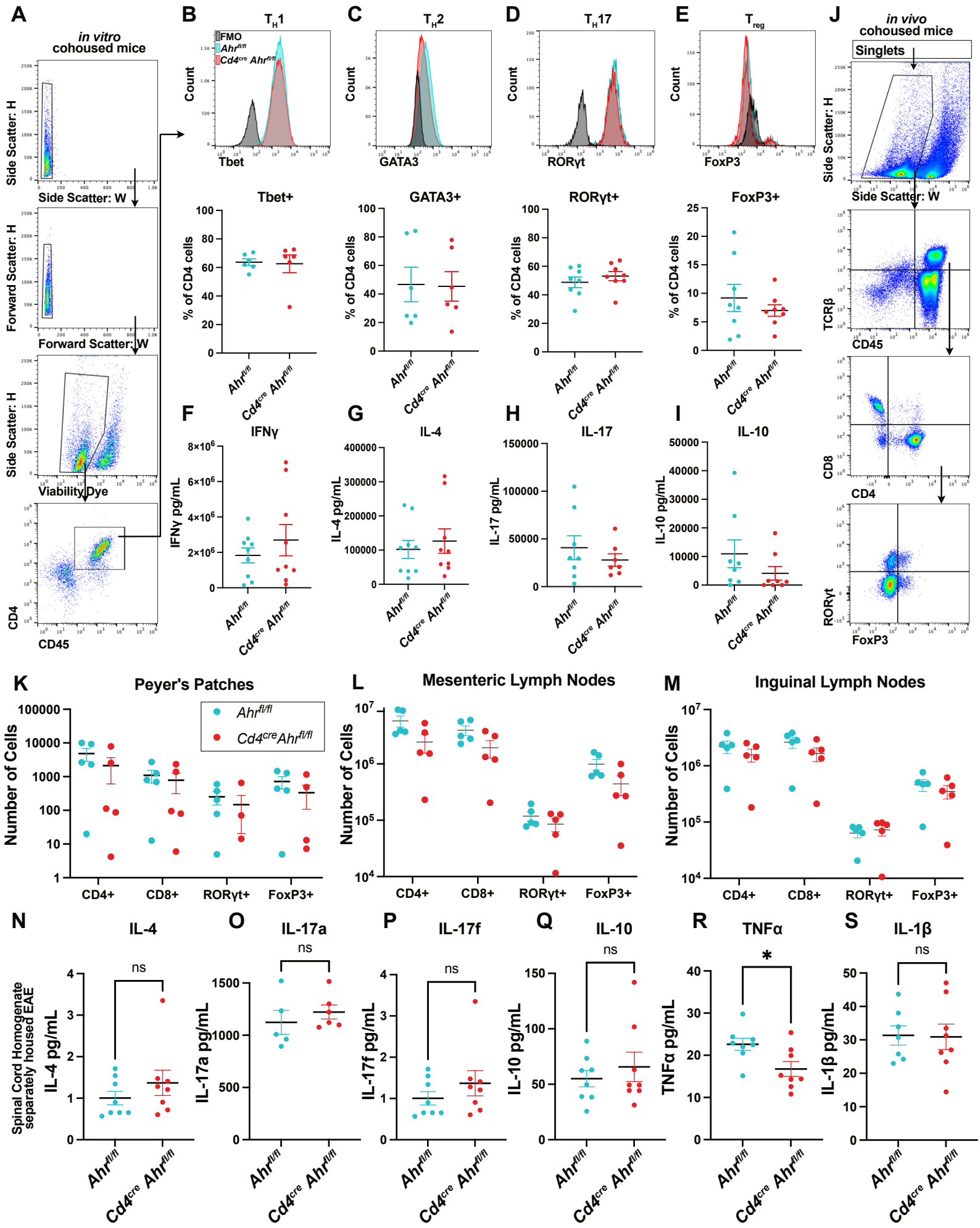
A
in vitro
cohoused mice
Side Scatter: H
Side Scatter: W
Forward Scatter: H
Forward Scatter: W
Side Scatter: H
Viability Dye
CD4
CD45
B
T_H1
FMO
Ahr^fl/fl
Cd4^cre Ahr^fl/fl
Count
Tbet
Tbet+
% of CD4 cells
C
T_H2
GATA3
GATA3+
D
T_H17
RORγt
RORγt+
E
T_reg
FoxP3
FoxP3+
J
in vivo
cohoused mice
Singlets
Side Scatter: H
Side Scatter: W
TCRβ
CD45
CD8
CD4
RORγt
FoxP3
F
IFNγ
IFNγ pg/mL
G
IL-4
IL-4 pg/mL
H
IL-17
IL-17 pg/mL
I
IL-10
IL-10 pg/mL
K
Peyer's Patches
Ahr^fl/fl
Cd4^cre Ahr^fl/fl
Number of Cells
CD4+
CD8+
RORγt+
FoxP3+
L
Mesenteric Lymph Nodes
M
Inguinal Lymph Nodes
N
IL-4
ns
O
IL-17a
ns
P
IL-17f
ns
Q
IL-10
ns
R
TNFα
*
S
IL-1β
ns
Spinal Cord Homogenate
separately housed EAE
IL-4 pg/mL
IL-17a pg/mL
IL-17f pg/mL
IL-10 pg/mL
TNFα pg/mL
IL-1β pg/mL

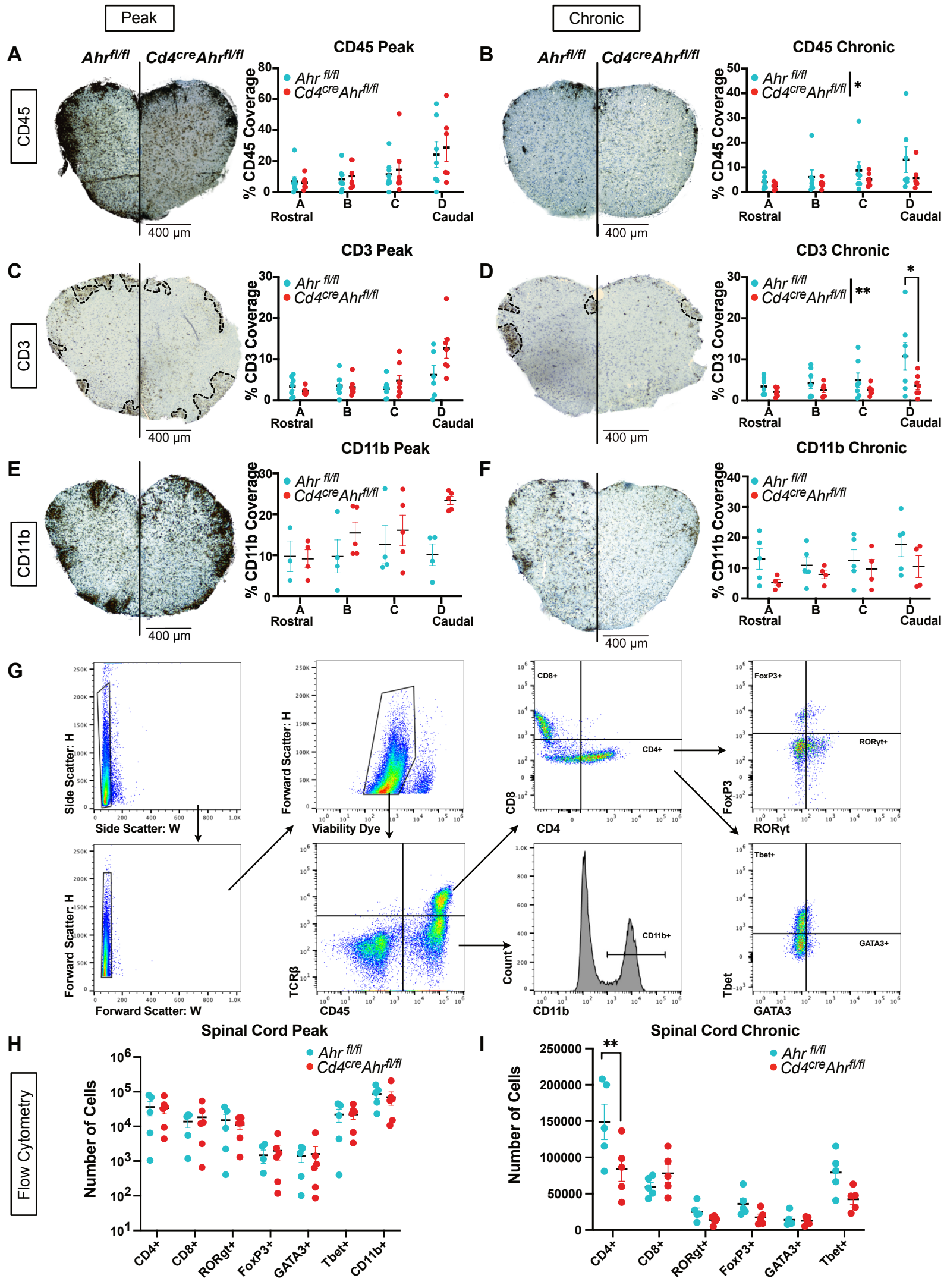
Peak
Chronic
A
B
C
D
E
F
G
H
I
CD45
CD3
CD11b
Ahrfl/fl
Cd4creAhrfl/fl
400 µm
CD45 Peak
CD45 Chronic
CD3 Peak
CD3 Chronic
CD11b Peak
CD11b Chronic
% CD45 Coverage
% CD3 Coverage
% CD11b Coverage
Rostral
Caudal
Side Scatter: H
Side Scatter: W
Forward Scatter: H
Forward Scatter: W
Viability Dye
TCRβ
CD45
CD8
CD4
CD8+
CD4+
FoxP3
FoxP3+
RORγt
RORγt+
Count
CD11b
CD11b+
Tbet
Tbet+
GATA3
GATA3+
Flow Cytometry
Spinal Cord Peak
Spinal Cord Chronic
Number of Cells
CD4+
CD8+
RORgt+
FoxP3+
GATA3+
Tbet+
CD11b+

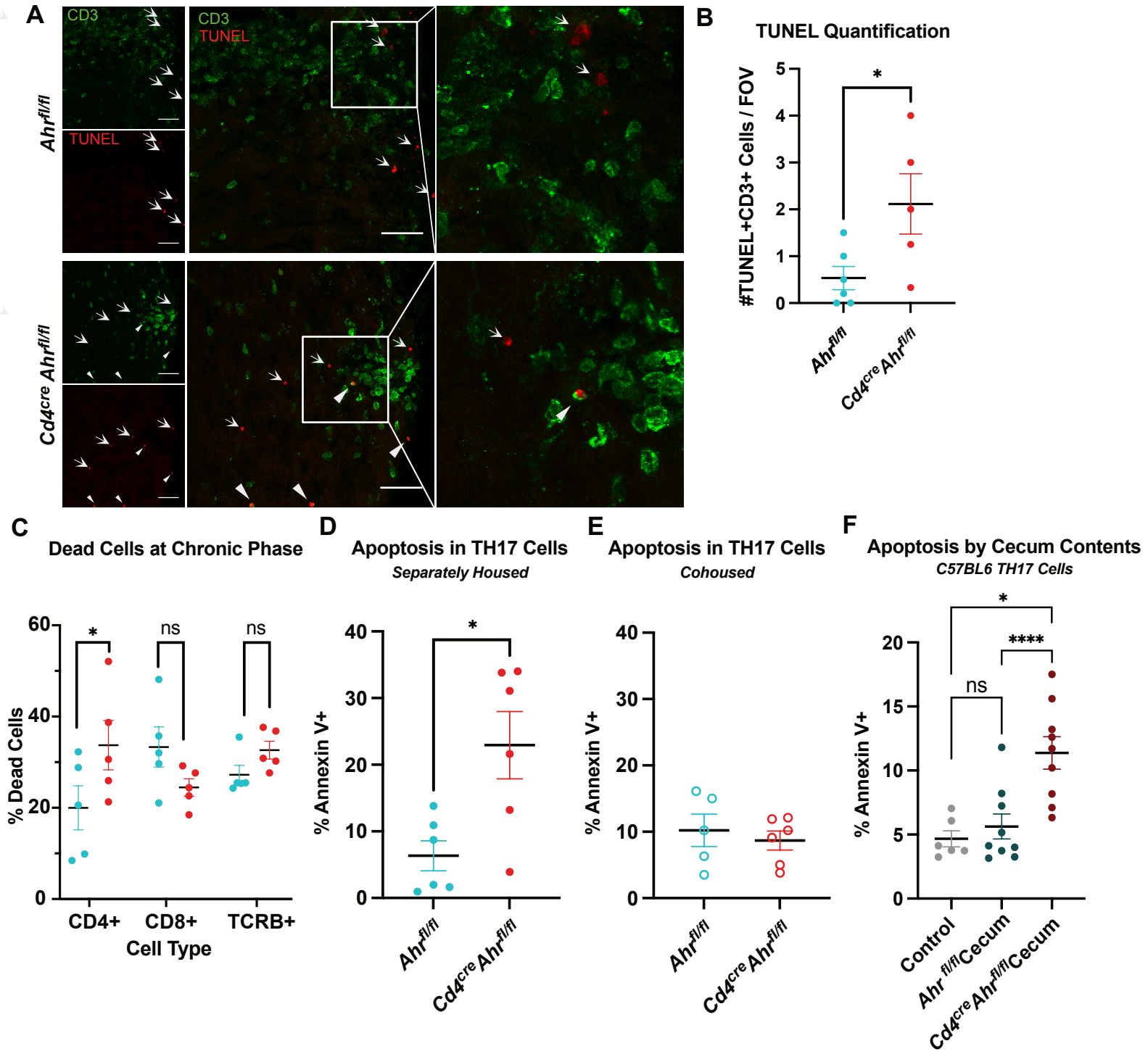
A
CD3
TUNEL
CD3
TUNEL
Ahr fl/fl
Cd4cre Ahr fl/fl
B
TUNEL Quantification
#TUNEL+CD3+ Cells / FOV
*
Ahr fl/fl
Cd4cre Ahr fl/fl
C
Dead Cells at Chronic Phase
% Dead Cells
*
ns
ns
CD4+
CD8+
TCRB+
Cell Type
D
Apoptosis in TH17 Cells
Separately Housed
% Annexin V+
*
Ahr fl/fl
Cd4cre Ahr fl/fl
E
Apoptosis in TH17 Cells
Cohoused
% Annexin V+
Ahr fl/fl
Cd4cre Ahr fl/fl
F
Apoptosis by Cecum Contents
C57BL6 TH17 Cells
% Annexin V+
*
****
ns
Control
Ahr fl/fl Cecum
Cd4cre Ahr fl/fl Cecum

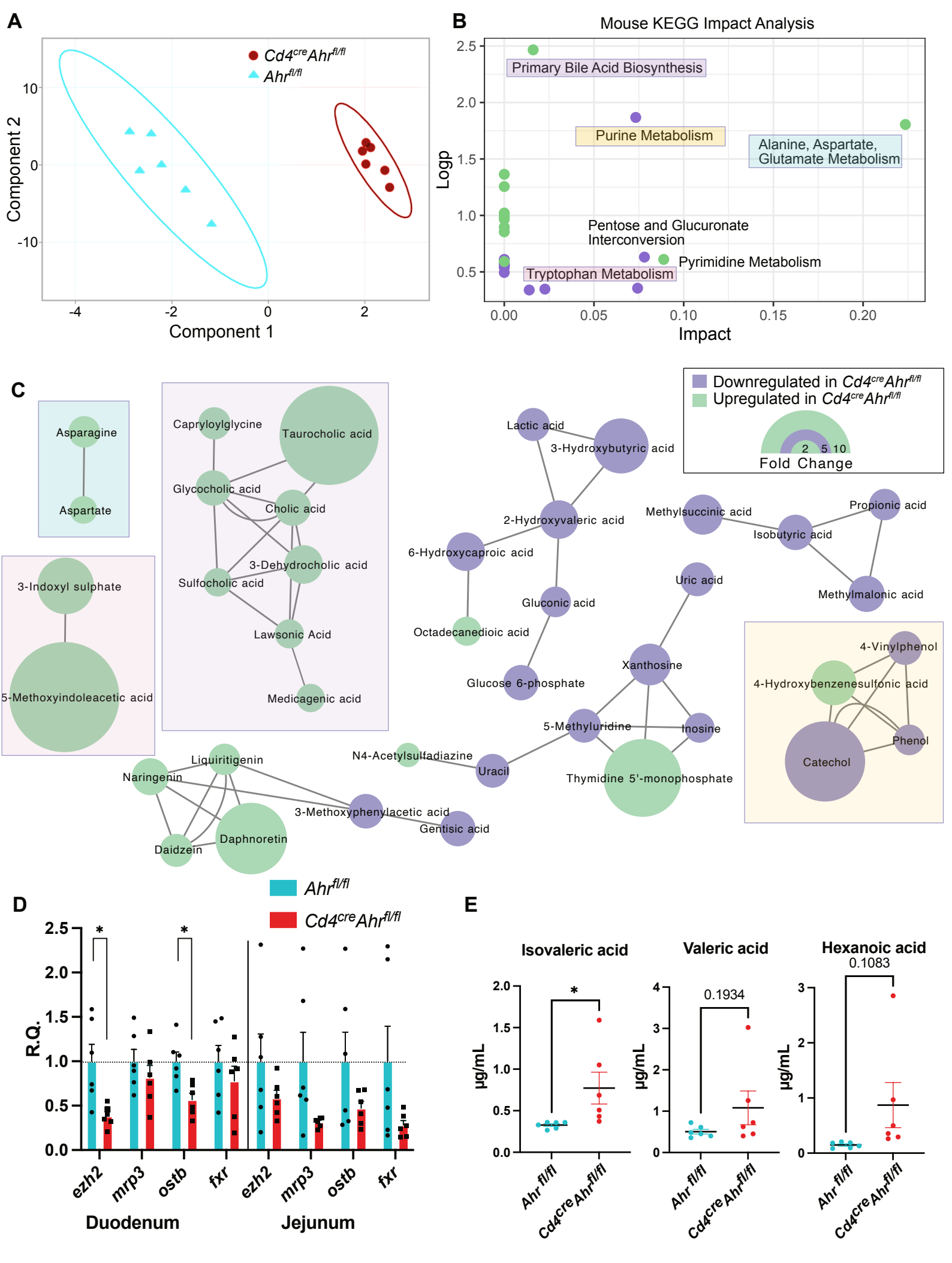
A
Cd4cre Ahrfl/fl
Ahrfl/fl
Component 2
Component 1
B
Mouse KEGG Impact Analysis
Primary Bile Acid Biosynthesis
Purine Metabolism
Alanine, Aspartate, Glutamate Metabolism
Pentose and Glucuronate Interconversion
Pyrimidine Metabolism
Tryptophan Metabolism
Logp
Impact
C
Downregulated in Cd4cre Ahrfl/fl
Upregulated in Cd4cre Ahrfl/fl
Fold Change
Asparagine
Aspartate
Capryloylglycine
Taurocholic acid
Glycocholic acid
Cholic acid
3-Dehydrocholic acid
Sulfocholic acid
Lawsonic Acid
Medicagenic acid
3-Indoxyl sulphate
5-Methoxyindoleacetic acid
Lactic acid
3-Hydroxybutyric acid
2-Hydroxyvaleric acid
6-Hydroxycaproic acid
Gluconic acid
Octadecanedioic acid
Glucose 6-phosphate
Methylsuccinic acid
Propionic acid
Isobutyric acid
Methylmalonic acid
Uric acid
Xanthosine
5-Methyluridine
Inosine
Thymidine 5'-monophosphate
Uracil
N4-Acetylsulfadiazine
4-Vinylphenol
4-Hydroxybenzenesulfonic acid
Phenol
Catechol
Liquiritigenin
Naringenin
Daphnoretin
Daidzein
3-Methoxyphenylacetic acid
Gentisic acid
D
Ahrfl/fl
Cd4cre Ahrfl/fl
R.Q.
ezh2
mrp3
ostb
fxr
Duodenum
Jejunum
E
Isovaleric acid
Valeric acid
Hexanoic acid
0.1083
0.1934
μg/mL
Ahr fl/fl
Cd4cre Ahrfl/fl

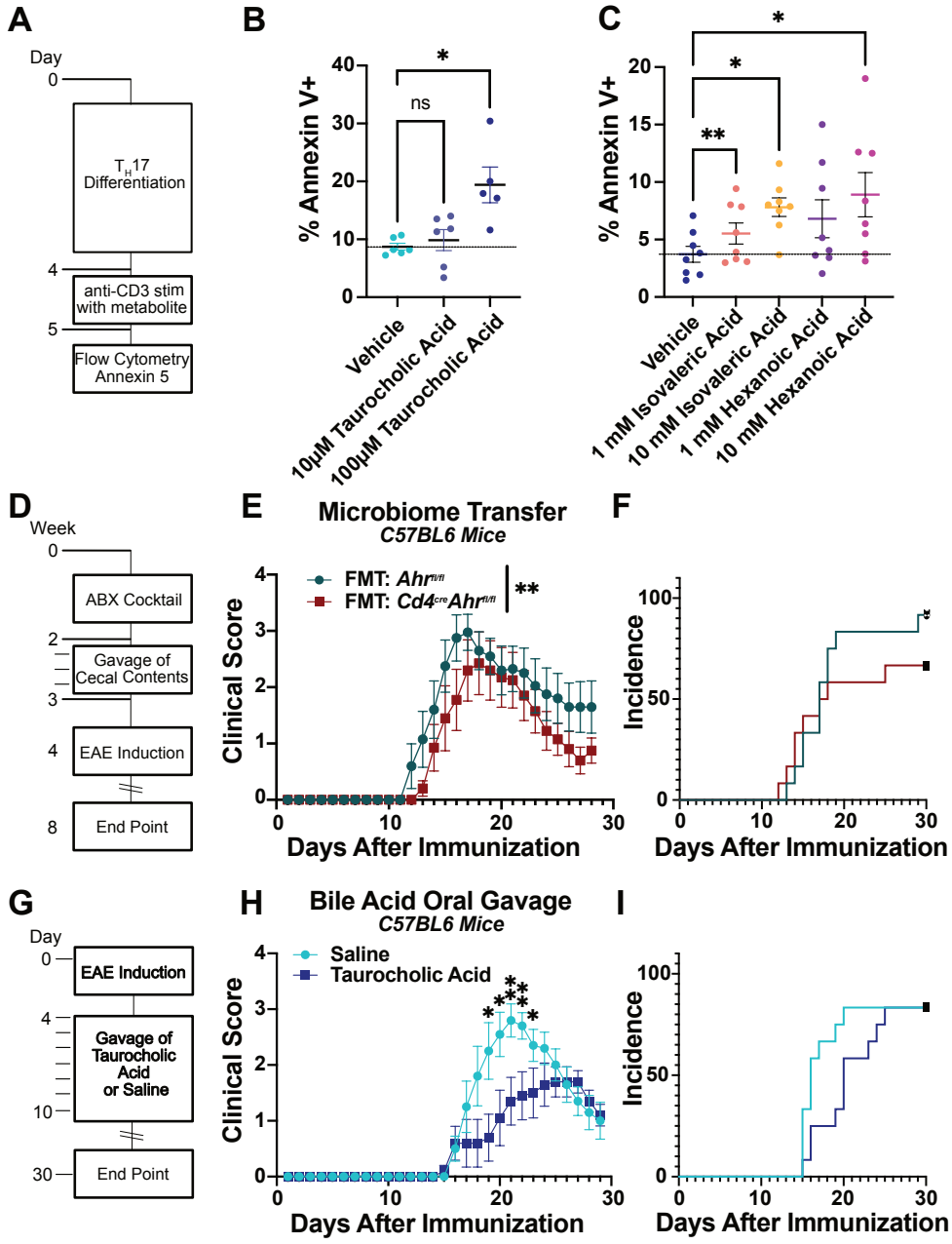
A
Day
0
T_H17 Differentiation
4
anti-CD3 stim with metabolite
5
Flow Cytometry Annexin 5
B
% Annexin V+
ns
*
Vehicle
10μM Taurocholic Acid
100μM Taurocholic Acid
C
% Annexin V+
**
*
*
Vehicle
1 mM Isovaleric Acid
10 mM Isovaleric Acid
1 mM Hexanoic Acid
10 mM Hexanoic Acid
D
Week
0
ABX Cocktail
2
Gavage of Cecal Contents
3
4
EAE Induction
8
End Point
E
Microbiome Transfer
C57BL6 Mice
FMT: Ahr fl/fl
FMT: Cd4cre Ahr fl/fl
**
Clinical Score
Days After Immunization
F
Incidence
Days After Immunization
G
Day
0
EAE Induction
4
Gavage of Taurocholic Acid or Saline
10
30
End Point
H
Bile Acid Oral Gavage
C57BL6 Mice
Saline
Taurocholic Acid
Clinical Score
Days After Immunization
I
Incidence
Days After Immunization